

Ionic wind amplifier for energy-efficient air propulsion: Prototype design, development, and evaluation

Donato Rubinetti^{a,b,*}, Kamran Iranshahi^{a,c}, Daniel Onwude^a, Julien Reymond^{a,d},
Amirmohammad Rajabi^{a,d}, Lei Xie^e, Bart Nicolai^b, Thijs Defraeye^{a,f,**}

^a Empa, Swiss Federal Laboratories for Materials Science and Technology, Laboratory for Biomimetic Membranes and Textiles, Lerchenfeldstrasse 5, CH-9014, St. Gallen, Switzerland

^b KU Leuven, BIOSYST-MeBioS, Willem de Croylaan 42, Heverlee, Belgium

^c HSLU, Lucerne School of Engineering and Architecture, Institute of Mechanical Engineering and Energy Technology IME, Technikumstrasse 21, CH-6048, Horw, Switzerland

^d EPFL, Swiss Federal Institute of Technology Lausanne, CH-1015, Lausanne, Switzerland

^e Belimed AG, Grienbachstrasse 11, CH-6300, Zug, Switzerland

^f Food Quality and Design, Wageningen University & Research, P.O. Box 17, 6700 AA, Wageningen, the Netherlands

ARTICLE INFO

Keywords:

Air propulsion

Air amplifier

Electrohydrodynamics

Ionic wind

Corona discharge

CFD

ABSTRACT

Ionic wind, produced by electrohydrodynamic (EHD) processes, holds promise for efficient airflow generation using minimal power. However, practical applications have been limited by relatively low flow rates. This study introduces a novel prototype device designed to amplify ionic wind-generated flow rates by leveraging the Coanda effect. This scalable device features a unique needle electrode configuration, optimized geometry, and operating parameters to enhance flow rates and reduce electrical energy consumption. The experimental investigation encompasses two ground electrode configurations as collectors to evaluate velocity profiles within an extended wind channel setup. The analysis revealed that the rod collector arrangement slightly outperformed the plate collector regarding airflow rate and efficiency. Notably, a flow rate of up to $7.5 \text{ m}^3 \text{ h}^{-1}$ was attained with an energy input of less than 2 W at 30 kV and a flow rate of $5 \text{ m}^3 \text{ h}^{-1}$ within the optimal voltage range of 15–20 kV, requiring around 0.5 W. The findings indicate that a decrease in the number of needle emitters has a relatively negligible impact on the airflow rate, suggesting an opportunity to design more efficient devices with fewer needles. To complement the experimental results, a computational fluid dynamics (CFD)-based digital mirror was utilized to obtain deeper insights into the flow field patterns. The use of the CFD model confirmed that our device can increase flow rates by a factor of around three. The findings of this research have far-reaching implications for developing next-generation ionic wind generators, particularly in sustainable fluid flow engineering. By confirming the effectiveness of amplified ionic wind-based airflow, we provide a clear path for this technology to contribute to cleaner production practices across various industries. Ionic wind amplifiers show potential in applications requiring precise airflow control, such as data centers, cleanrooms, sterilization, or drying processes, where removing excess heat or maintaining specific conditions is essential.

1. Introduction

Ionic wind technology, or electrohydrodynamic (EHD) airflow, has emerged as an eco-friendly and sustainable alternative to conventional fans due to its potential to generate flow rates at little electrical cost and

precise airflow manipulation (Wang et al., 2013). Despite its advantages, the practical application of ionic wind has been limited by challenges such as achieving sufficient flow rates (Lin et al., 2018). Recent advancements and reviews in the field demonstrate the growing interest and potential of the technology (Lai, 2020). This potential has spurred

* Corresponding author. Empa, Swiss Federal Laboratories for Materials Science and Technology, Laboratory for Biomimetic Membranes and Textiles, Lerchenfeldstrasse 5, CH-9014, St. Gallen, Switzerland.

** Corresponding author. Empa, Swiss Federal Laboratories for Materials Science and Technology, Laboratory for Biomimetic Membranes and Textiles, Lerchenfeldstrasse 5, CH-9014, St. Gallen, Switzerland.

E-mail addresses: donato.rubinetti@empa.ch (D. Rubinetti), thijs.defraeye@empa.ch (T. Defraeye).

<https://doi.org/10.1016/j.clet.2024.100728>

Received 11 October 2023; Received in revised form 19 December 2023; Accepted 23 January 2024

Available online 4 February 2024

2666-7908/© 2024 Published by Elsevier Ltd. This is an open access article under the CC BY-NC-ND license (<http://creativecommons.org/licenses/by-nc-nd/4.0/>).

research and development across various applications, such as energy-efficient thermal management (Zhang et al., 2022), (Venkatesh et al., 2021), (Ramadhan et al., 2017a), sustainable drying of sensitive materials (Defraeye and Martynenko, 2018), (Iranshahi et al., 2022), (Martynenko and Kudra, 2016) (Iranshahi et al. (2023), and even the intriguing demonstration of an emissionless ionic aircraft (Xu et al., 2018).

Ionic wind arises from a phenomenon wherein a high voltage applied to a sharp electrode (emitter) generates a corona discharge, ionizing the surrounding air and producing a mix of positive and negative ions (Monrolin et al., 2018). The subsequent Coulomb force drives these ions toward an oppositely charged electrode, often a grounded electrode (collector). During this process, the ions collide with neutral air molecules, transferring momentum and creating a flow of air – known as ionic wind or EHD flow. The strength of the ionic wind depends on the applied voltage, electrode sharpness, and electrode arrangement, regardless of the ambient parameters (Jewell-Larsen et al., 2006), (Zeng et al., 2023). Several researchers have focused on enhancing the speed of ionic wind. Significant advancements have been achieved through the optimization of emitter-collector arrangements (Johnson et al., 2015), (Tirumala and Go, 2011), (Zhang and Yang, 2021), including innovative bipolar configurations for microfluidic devices (Dinh et al., 2017), (Dau et al., 2016a). Further investigations include the application of nano-material coatings on emitters to increase discharge surface area (Wu et al., 2017), system designs comprising multiple EHD pumps (Kana-zawa et al.), (Rickard et al., 2006), and the integration of electrodes in symmetric arrangements for charge neutralization in the airstream (Dau et al., 2016b). Alternatively, some approaches aim to utilize magnetic fields in conjunction with electric fields to enhance acceleration through the Lorentz force (Wang et al., 2021), (Zhou et al., 2018). Shifting focus from these electrical improvements, a new area has emerged that concentrates on aerodynamic improvements. Central to this new direction is the ‘EHD air amplifier’ (Rubinetti et al., 2023a), designed to boost flow rates by utilizing ionic wind jets as bleed flow to induce a larger bulk flow through the Coanda effect (Rubinetti et al., 2023b). The Coanda effect is an aerodynamic phenomenon where a fluid jet adheres to a nearby surface due to near-wall pressure asymmetries, entraining surrounding fluid to create a more substantial flow (Panitz and Wasan, 1972), (Dumitrache et al., 2012). This approach of enhancing the airflow aspect of ionic wind with an air-amplifying mechanism represents a largely unexplored yet promising direction in ionic wind technology. The innovative and significant aspect of the present work is the creation of a scalable, rigorously tested prototype that bridges the gap between proof-of-concept and a viable ionic wind amplifier device, thereby paving the way for more effective and practical applications of ionic wind technology.

The potential impact of ionic wind amplifiers on various industries is substantial. For instance, in the heating, ventilation, and air conditioning (HVAC) industry, the technology could lead to energy savings and reduced operational costs by providing a low-cost air distribution and circulation technology (Chua et al., 2013), (Zhang and Li, 2020), (Ambaw et al., 2014). In electronics, efficient cooling of components could prolong the lifespan of devices, minimize the risk of overheating, and increase overall energy efficiency (Shao et al., 2022). Advances in needle plasma actuators and bipolar configurations have further demonstrated their potential in convective cooling applications, significantly improving heat transfer efficiencies (Zhao et al., 2015). Furthermore, in agriculture and food processing, the amplifier could facilitate precise and energy-efficient drying or aeration of crops, reducing energy consumption and environmental impact (Onwude et al., 2021). In addition to its energy efficiency, ionic wind technology offers several environmental benefits, making it an ideal candidate for cleaner production practices. The absence of moving parts results in significantly reduced noise pollution compared to conventional fans (Vaddi et al., 2020), (Zhao and Adamiak, 2016), providing a more comfortable environment in noise-sensitive areas, such as offices or

residential buildings. Unlike conventional air amplifiers, which rely on a source of pressurized air, the ionic wind amplifier operates independently, offering a unique advantage in self-sufficiency and system simplicity. Despite its potential and numerous proposed devices (Johnson and Go, 2017), (Qu et al., 2021), there remains a lack of commercially available products effectively harnessing the advantages of ionic wind technology, including low energy consumption and decentralized airflow. A key obstacle is the low flow rates and the slight rise in pressure associated with ionic wind technology (Jewell-Larsen et al., 2011). Innovative solutions to these challenges have been proposed, including structural and functional improvements detailed in recent publications (Rubinetti et al., 2023a), (Rubinetti et al., 2023b) and patent filings (Xie et al., 2023). These documents demonstrate the ongoing efforts to refine and commercialize this emerging technology.

In this study, we build upon the previous work and propose an experimental concept for an ionic wind prototype that is 179 mm long and has an inner cross-section of 70×50 mm, which is a 2D design and scalable for customizability in specific applications. To comprehensively evaluate the system, we investigate two different electrode spacings (20 mm and 30 mm) and compare the effects of using rod and plate types as collector electrodes. This approach is informed by findings that the proximity of dielectric materials or other structures near the emitting electrode can significantly influence the ion wind generation, potentially affecting the system's charge/discharge dynamics and overall efficiency (Rubinetti et al., 2023b). This study aims to advance EHD adoption and position it as an environmentally friendly airflow generation technology. We characterize the performance of the ionic wind amplifier and provide experimental data to further the development of practical applications for ionic wind technology. We built a prototype device with a unique electrode configuration and optimized operating parameters. We measured its velocity profile in an extended channel. Furthermore, we constructed a CFD-based digital mirror, a virtual replica of the ionic wind channel, to validate the experimental data and extract additional flow field data, such as the device's amplification factor and flow fields.

2. Technological principle of ionic wind amplification

Ionic wind amplification, or EHD air amplification, is an innovative technique that leverages electrostatic principles to generate amplified airflow without additional electrical costs. As illustrated in Fig. 1, the ionic wind amplification process is based on two interconnected phenomena: the corona discharge and the Coanda effect. In the first step, a high voltage is applied to sharp emitter electrodes within side channels, as shown in Fig. 1a. This high voltage generates a corona discharge, which ionizes air molecules and creates positive and negative ions. The charged ions are then attracted toward the oppositely charged collector electrodes, resulting in the movement of ions through the side channels. The motion of these charged ions in the side channels gives rise to an ionic wind jet, as depicted in Fig. 1b. The ionic wind jet consists of a high-velocity, low-pressure air stream that remains attached to the side channel wall due to the Coanda effect. The Coanda effect is an aerodynamic phenomenon in which a fluid jet adheres to a nearby surface because of pressure asymmetries, entraining the surrounding fluid and generating a more substantial flow. In the case of ionic wind amplification, the ionic wind jet generated in the side channel adheres to the main channel wall, inducing a larger bulk flow. This amplified airflow results from the induction of surrounding air, driven by the pressure differences created by the Coanda effect. As such, the air is entrained, and the airflow rate generated by the ionic wind is multiplied. It is worth noting that the primary acceleration is strictly confined to the space between the electrodes without additional momentum-inducing elements. The charged molecules experience acceleration via the Coulomb force, a product of space charge and electric field. In addition, the channel geometry contains the necessary elements for air amplification, including a converging nozzle and a Coanda surface (Rubinetti et al.,

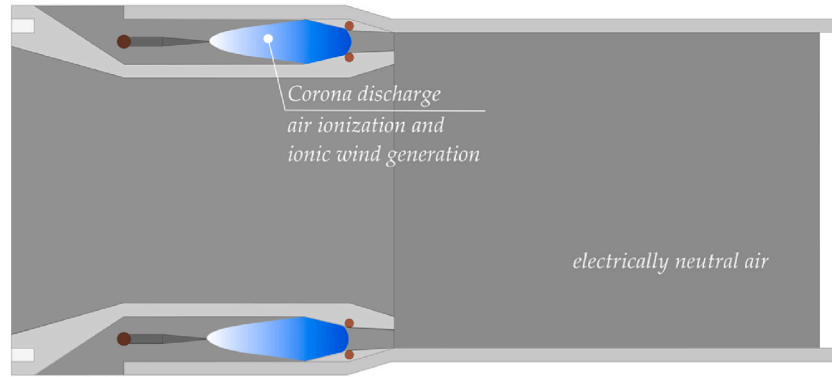
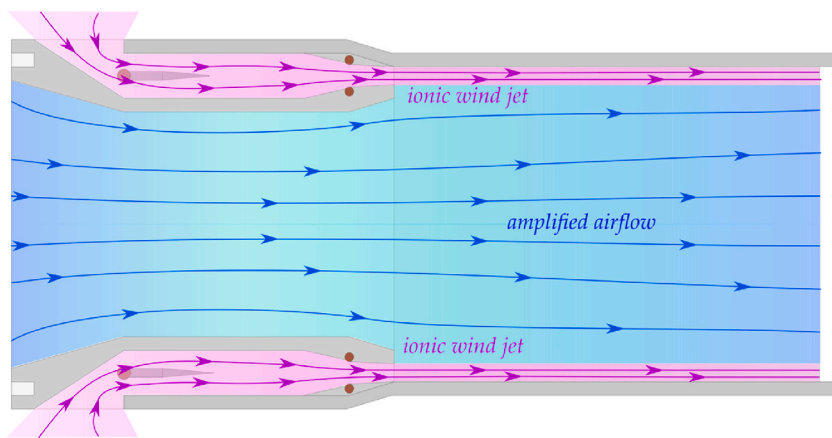
a Configuration v2 electrostatic principle**b** Configuration v2 aerodynamic principle

Fig. 1. Ionic wind amplification, or EHD air amplification, is based on two interconnected phenomena. The first is the electrostatic principle, illustrated in Subfigure (a), where a corona discharge occurs in the side channels. This corona discharge generates an ionic wind jet, as depicted in Subfigure (b). As the ionic wind jet remains attached to the wall through the Coanda effect, it induces a larger airflow, creating amplified airflow.

2023a). Consequently, the ionic wind amplification process generates a larger airflow than possible using only the ionic wind jet. Furthermore, the enclosed design of the system provides a protective shield for all electrical components, ensuring a safer environment for high-voltage engineering-related challenges like electrical shielding and arcing.

3. Materials and methods

3.1. Device construction

As depicted in Fig. 2, the ionic wind amplifier unit consists of two main parts: the cover piece featuring the Coanda surface and the core part containing the electrical components. The two parts are assembled by sliding the cover piece over the core piece. The primary structure of the device is composed of laser-sintered polyamide reinforced with glass fiber (PA-GF), a material well-suited for 3D printing applications. Later, other manufacturing methods can be used to mass produce this device and allow the cost-effective production of the device. The electrical components, like the ground and needle holder, are copper, while the needles are crafted from tungsten. Tungsten was chosen for its corrosion-resistant properties, ensuring the longevity and reliability of the needles for discharge processes (Cogollo de Cádiz et al., 2021). The device contains four custom-shaped tungsten needles, specifically

designed and spaced to prevent spark over. The ideal needle shape, including tip curvature, has been determined in a previous study (Rubinetti et al., 2024). The needle shape follows a particular design that allows for a stable discharge in a constrained environment. The needles on either side of the device are connected in parallel via the copper-made needle holder.

Furthermore, the device's design can be easily enlarged by extruding in one direction to create a larger ionic wind amplifier for potential applications requiring a higher flow rate capacity. This modular approach offers flexibility and scalability, depending on the specific requirements of different use cases. This versatility in design makes the ionic wind amplifier adaptable to a wide range of applications, from small-scale localized cooling to large-scale ventilation systems.

3.2. Experimental setup

3.2.1. Test rig

The experimental test rig, illustrated in Fig. 3, was specifically designed to evaluate the performance of the ionic wind amplifier. The rig consists of a wind tunnel with flow straighteners attached in front and behind the ionic wind amplifier unit, ensuring uniform and high-quality airflow. The channel is constructed on a base attachment, where the ionic wind amplifier can be securely mounted onto aluminum

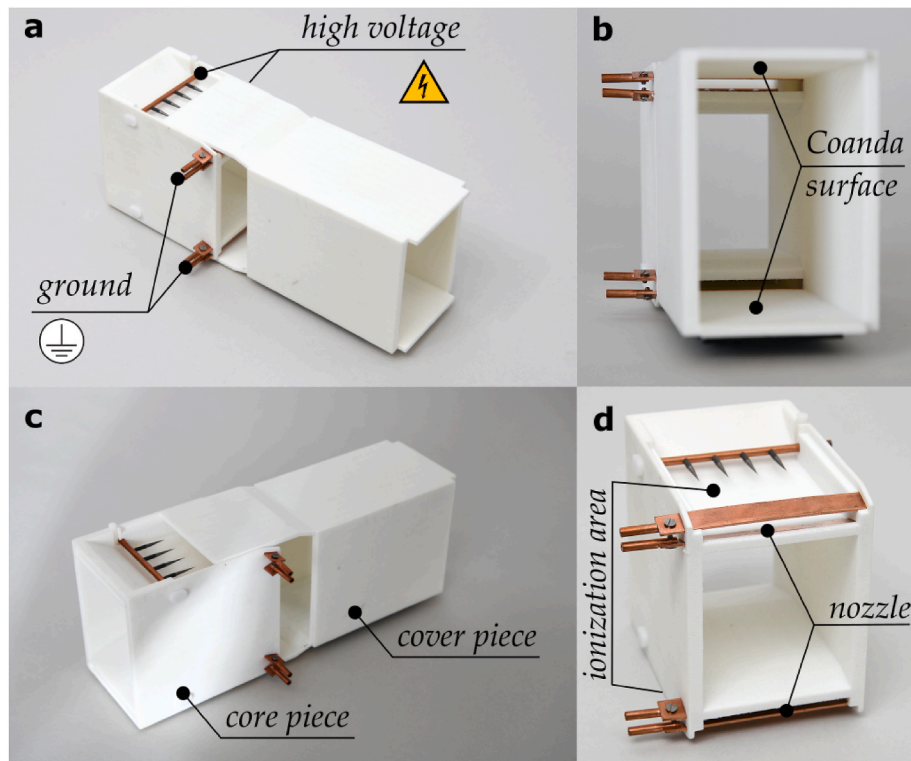


Fig. 2. A multi-angle view of the design and components of a single ionic wind amplifier device. The top view (a) of the partially opened unit indicates the primary electrical interfaces required for the device to function. The inside view (b) shows the internal structure and the Coanda surfaces that are important for the amplifying effect. (c) Displays the device's two essential components: the cover piece with the Coanda surface and the core piece with all conductive elements, including the needle arrangement. (d) Focuses solely on the core piece, highlighting the electrical components. The area between the grounded plates and the tungsten needles acts as the ionization and charge acceleration zones. The device comprises a mix of materials: the main structure is laser-sintered PA-GF, while the electrical components, including the grounded plates and needle holder, are made of copper. Because of its corrosion endurance and conductive characteristics, tungsten is utilized for needles. This design integrates multiple materials effectively to maximize the device's functionality.

profiles. To ensure safety during high voltage experiments, the entire setup is housed within a $1 \times 1 \times 2 \text{ m}^3$ high voltage safety box, which also functions as a Faraday cage. Outside the safety box, the ionic wind amplifier is connected to a DC-positive high-voltage power supply (Spellmann SL30PN10, 0–32 kV, 10 W). For accurate velocity profile measurements, the rear flow straightener features holes to accommodate a hot-wire anemometer (Testo 405i, Resolution 0.01 m s^{-1} , one data point per 1 s). The anemometer is mounted on a linear guide connected to an electric motor, enabling it to move at a constant speed. This setup allows for precise velocity profile recordings with an accuracy of 1.27 mm per second.

3.2.2. Ionic wind amplifier grounded electrode configurations

The ionic wind amplifier features two grounded electrode configurations, as shown in Fig. 4. The side channels in both configurations are 10 mm in height and converge to a nozzle with a 4 mm gap. This contraction ratio has been found to accelerate ionic wind jets while presenting minimal pressure resistance (Rubinetti et al., 2023b). At the end of the nozzle, the cover piece starts immediately and provides the Coanda surface. Multiple units can be stacked sequentially to create a larger ionic wind amplifier tunnel structure. Single units with flow straighteners and two and three sequential units were tested to understand the airflow capacity when multiple units were attached.

In configuration v1, illustrated in Fig. 4a, the grounded electrode is a copper plate (60 mm \times 8 mm \times 2 mm) collector embedded in the nozzle of the side channels, providing a larger charge deposition area. Configuration v2, depicted in Fig. 4b, uses a less exposed, embedded rod collector of 2 mm diameter, also made of copper, where only 0.9 mm of the surface is exposed. We expect configuration v2 to result in reduced energy consumption. The needle distance was chosen to generate

adequate airflow while preventing arcing based on previous experimental and numerical studies that revealed an interaction between the dielectric (here, the PA-GF structure) and the electric field (Rubinetti et al., 2023b).

Due to its high electrical conductivity, the needle holder and plate collector are made of copper. The chosen needle lengths of 20 mm and 30 mm interelectrode distance minimize the risk of sparkover caused by the denser electric field lines within the side channels, as shown in simulations we performed in a prior simulation study. The two ground configurations aim to test the effects of having the collector electrode more exposed to the surrounding air (configuration v1 with plate collectors) versus having the collector electrode primarily embedded within the structure (configuration v2 with rod collectors). The collectors are designed to have a significantly larger curvature than the needle tips to prevent the formation of secondary corona discharges.

The Coanda surface is straight, but we also tested a cover piece with a Coanda surface that bends away from the ionic wind jet, as seen in Fig. 5. This configuration investigates whether a larger back part, measuring 100 mm \times 50 mm at the outlet, increases the airflow and amplification factor. A corresponding rear flow straightener has been manufactured for this modified cover piece.

3.2.3. Experimental procedure

We conducted experiments to analyze the performance of two main ionic wind amplifier configurations, v1 and v2. These configurations can be seen in Fig. 4. Variables under investigation included electrode distance, Coanda surface shape, number of stages, and number of needles per side. We obtained measurements for electric current, temperature, humidity, and velocity profile. The relative humidity and ambient temperature were monitored with Sensirion SHT31 sensors (Sensirion,

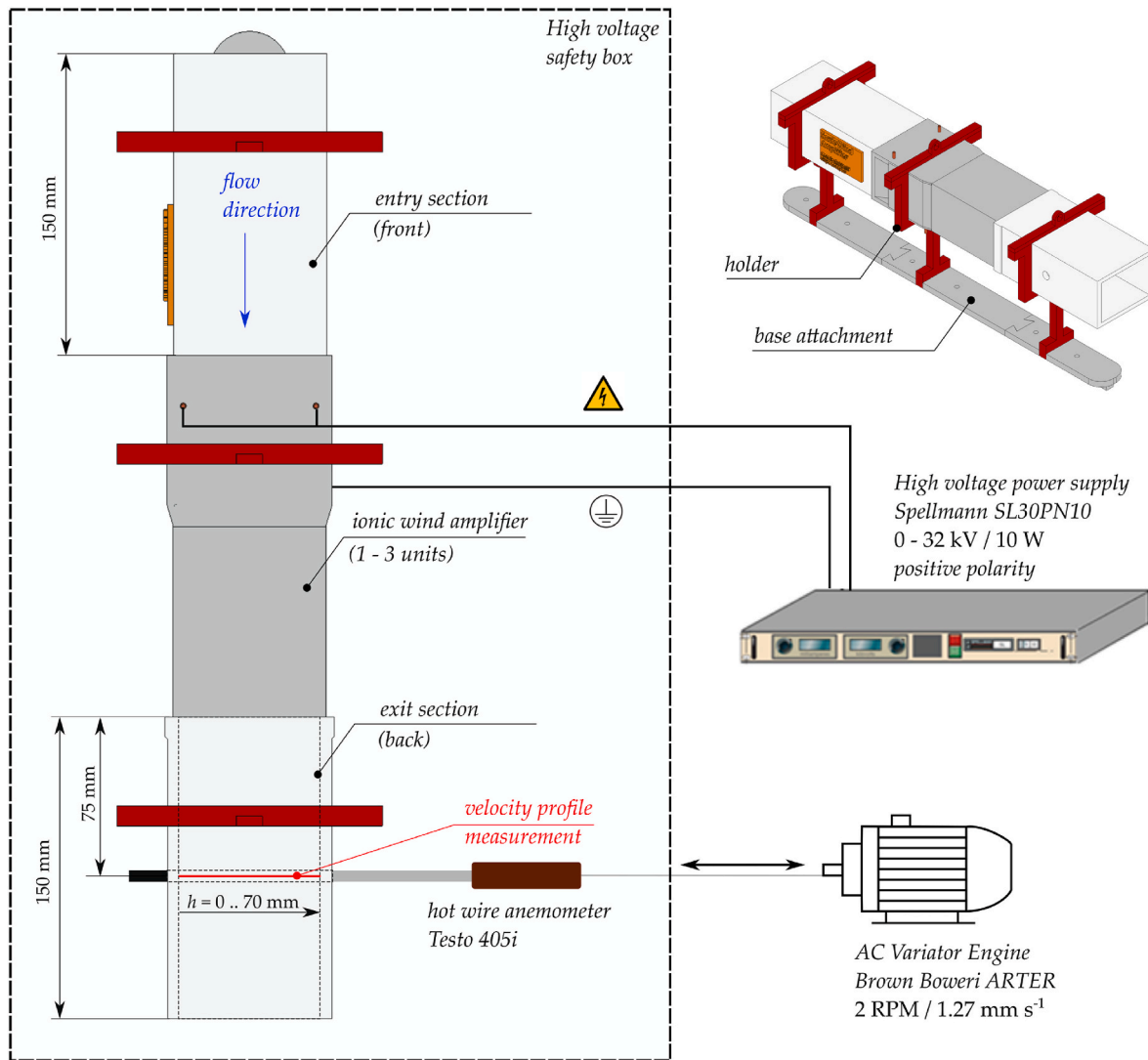


Fig. 3. Experimental test-rig for evaluating the ionic wind amplifier performance. Entry and exit sections are positioned before and behind the ionic wind amplifier unit. The channel is constructed on a base attachment with aluminum profiles for mounting the ionic wind amplifier. The setup is housed in a $1 \times 1 \times 2 \text{ m}^3$ high voltage safety box, which functions as a Faraday cage. The ionic wind amplifier is connected to an external high voltage power supply. The exit section features holes for a hot-wire anemometer to measure the velocity profile. The anemometer is mounted on a linear guide with an electric motor, enabling constant speed movement and velocity profile recordings with an accuracy of 1.27 mm per second.

Stäfa, Switzerland, accuracy of 2 % on relative humidity and 0.2°C on temperature). A Testo 405i anemometer (Testo SE & Co. KgaA, Celsiusstrasse 2, 79,822 Titisee-Neustadt. Accuracy 0.1 m s^{-1} , resolution 0.01 m s^{-1}) and an Apple iPad with iOS 16 were used for velocity profile measurements. The Testo Smartprobes app on the iPad sampled data at a frequency of 1 Hz. Three separate measurements are carried out at each location, i.e., at each data point along the measurement line. The ionic wind amplifier units were mounted vertically within a high voltage safety box, as shown in Fig. 3. They were placed between two flow straighteners. A base attachment was used for mounting the amplifier units. This attachment maintained a distance between the tunnel and the aluminum beams inside the box. The variator engine was calibrated before each experiment. This engine pulled the anemometer, which was mounted on a glide system. Electric current measurements were recorded manually during the experiments. The calibrated engine rotated at 2 rpm. This setup allowed for precise velocity profile measurements. After setting the voltage, the engine was connected to the glide system. The velocity profile was then measured. The anemometer was disconnected from the engine after exiting the rear flow straightener. It was pulled back in after a 1-min wait and reattached to the engine. The

voltage was incremented, and the measurement process was repeated.

Several variables and variations of the setup were tested. These variations are summarized in Table 1. Experiments with fewer needles were conducted to assess energy-saving potential. Since the flow rate results for the rod configurations were similar to those of the plate collector, we focused primarily on variations in rod configurations, deeming it unnecessary to perform the full range of variations on both configurations. Each experimental run was performed three times. Safety precautions were taken during the experiments.

3.3. Computational fluid dynamics (CFD) digital mirror

The purpose of the CFD digital mirror, a reflective representation of the real-world setup, is to provide additional data to complement experiments, focusing primarily on the fluid flow aspect alone. Unlike a 'digital twin', which is a real-time virtual representation encompassing all physical behaviors and reactive changes, our 'digital mirror' is a more focused tool. It is calibrated directly against experimental data, serving as a reflective model of the specific dataset rather than replicating the entire physical system. By employing a digital mirror, we can acquire

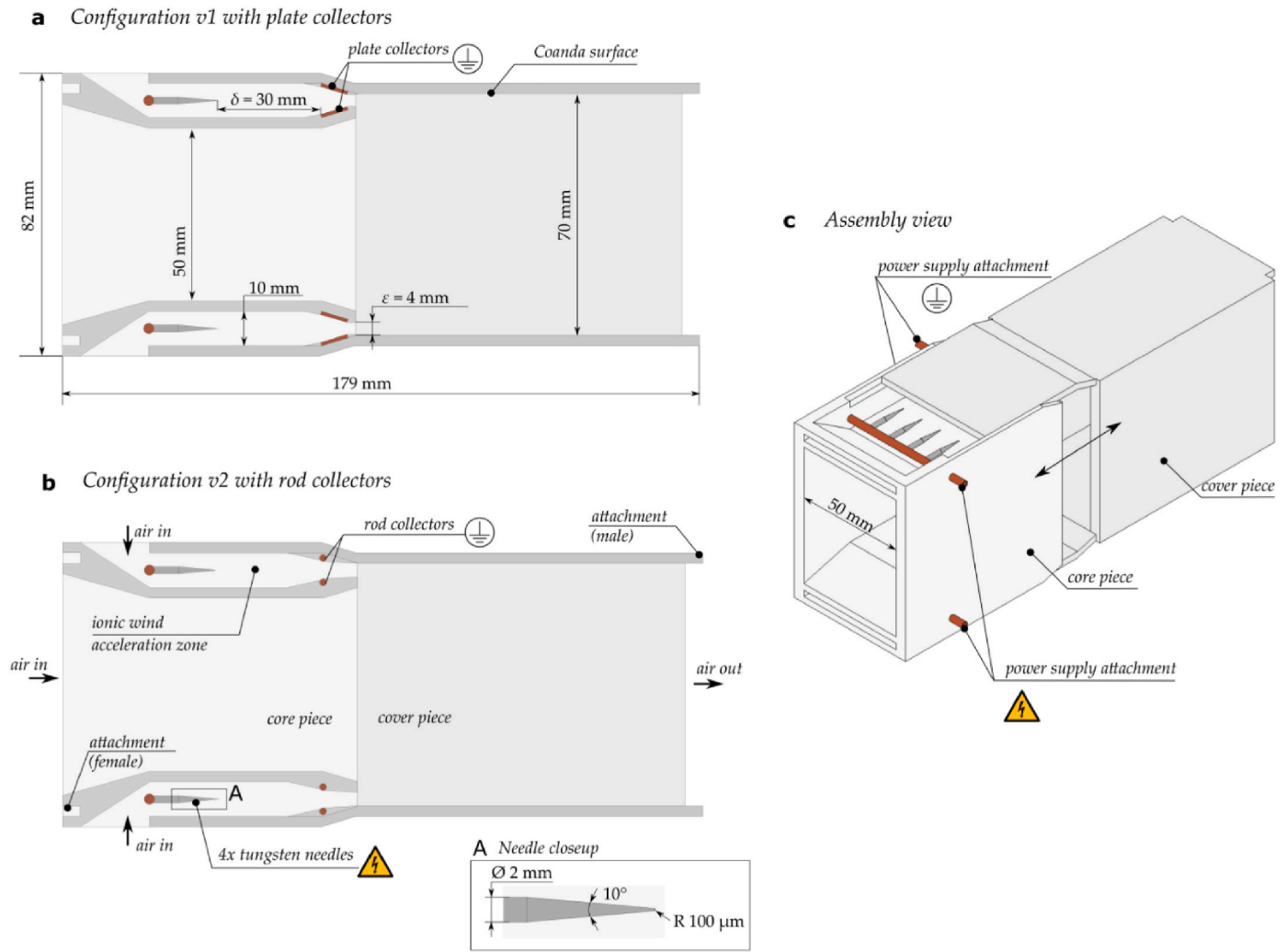


Fig. 4. The ionic wind amplifier has two configurations. The first configuration, v1, according to (a), uses plate collectors as ground electrodes. The second configuration, represented by (b), uses embedded rod collectors as ground electrodes. Both configurations consist of a core piece, where the electrical components are installed, and a cover piece. Subfigure (c) shows the assembly view. The emitter needle has a specific shape and tip curvature to minimize electric power consumption while increasing airflow speed and improving discharge stability (Rubinetti et al., 2024).

Configuration v2 with rod collectors and curved cover piece

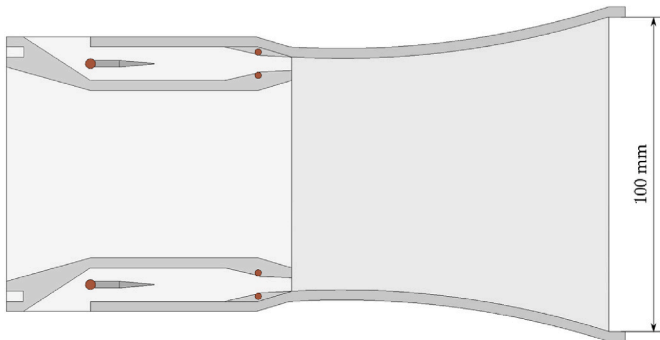


Fig. 5. Configuration v2 with rod collectors and a cover piece featuring curved surfaces instead of straight ones.

valuable insights into the fluid flow behavior and extend the experimental results to obtain flow fields and metrics like the amplification factor. This eliminates the need for modeling the complex electrostatic interactions of corona discharge, which are characterized by significant non-linearities and high computational demands. This complementary

information is handy in cases where direct measurements are not feasible, such as determining the inlet velocity of the lateral inlets. Such a procedure would be experimentally infeasible, as the introduction of measurement instruments could alter the electric field and severely disturb the discharge process, potentially leading to premature spark-over. Our CFD model specifically addresses the airflow dynamics within the ionic wind amplifier, rather than the charge generation and discharge current. This decision stems from the significant complexity and computational challenges in accurately simulating the electrostatic components in a 3D space. As such, the governing equations and boundary conditions for the electric field and charge transport are not included in our digital mirror.

3.3.1. 3D geometry

The digital mirror 3D geometry closely matches the ionic wind amplifier's dimensions, as illustrated in Fig. 6. We import the CAD data into the simulation software. This data contains intricate details such as needles and needle holders. After setting up the geometry, we fill the space inside the domain with air. This acts as the working fluid. We simplify the model by applying symmetry conditions to save computational time and resources. This effectively reduces the domain to a quarter of its original size. This method effectively depicts fluid flow behavior within the ionic wind amplifier.

Table 1

Characteristics of the measurements.

Config.	Regulated variables and variations					Measured variables			
	Voltage	Electrode distance	Coanda surface shape	Number of stages	Number of needles per side	Electric Current	Temperature	Humidity	Velocity profile
	U [kV]	δ [mm]		#	#	I [μ A]	T [$^{\circ}$ C]	φ [%]	w [m/s]
v1 plate	10–30	30	Straight	1	4	✓	✓	✓	✓
v2	10–30	30	Straight	1	4				
rod	10–30	30	Straight	1	4/2/1				
	10–30	30	Straight	1/2/3	4				
	10–30	30/20	Straight	1	4				
	10–30	30	Curved	1	4				

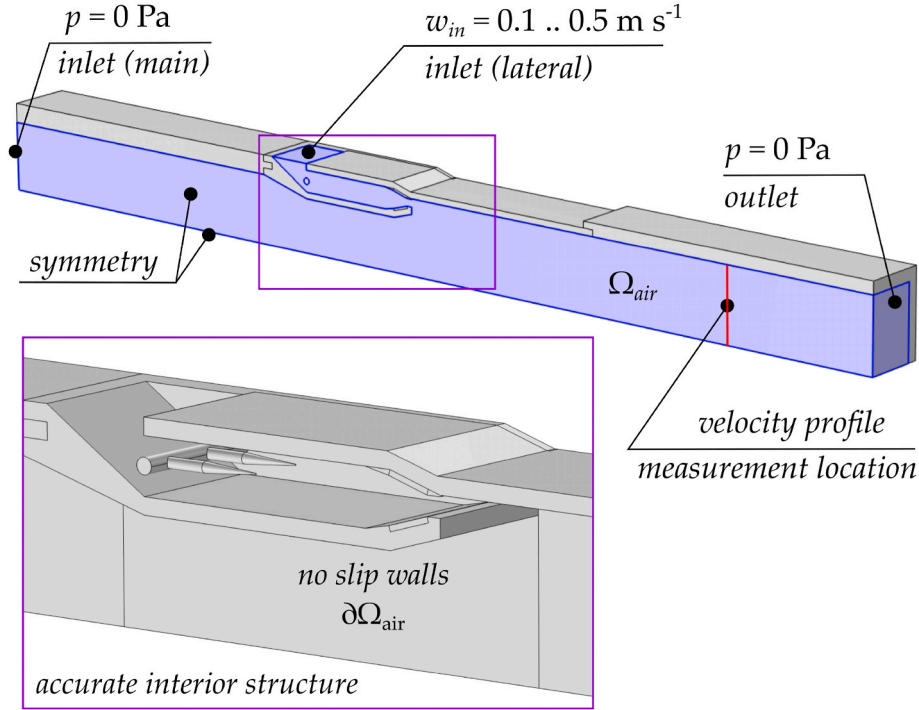


Fig. 6. The digital mirror geometry accurately replicates the dimensions of the ionic wind amplifier. The CAD data is imported into the simulation software. The CFD model accounts for fine details of the interior structure, including needles and needle holders. To optimize computational time, symmetry conditions are applied, reducing the model to a quarter of the entire domain.

3.3.2. Turbulent CFD model

The Navier-Stokes momentum equation describes the incompressible airflow within the ionic wind amplifier:

$$\rho \mathbf{u} \bullet \nabla \mathbf{u} = -\nabla p + \mu \nabla^2 \mathbf{u} \quad (1)$$

Here, ρ represents air density [kg m^{-3}], \mathbf{u} denotes the velocity field [m s^{-1}], p stands for pressure [Pa], and μ is the dynamic viscosity [Pa s]. We employ a Reynolds-averaged Navier Stokes (RANS) method in the airflow model, selecting the standard $k-\epsilon$ turbulence model to characterize non-laminar behavior in the CFD. A turbulence intensity of 5% is determined to offer the best stability in Coanda-effect-driven airflows.

Various alternative models are examined, including e.g., $k-\omega$, SST, and $v2f$, all with and without wall functions. The choice of the turbulence model and the reasoning behind it are elaborated in (Rubinetti et al., 2023a). In these investigations, the mesh near the walls was refined adequately to yield dimensionless wall distance values y^+ of around 1. This high level of refinement ensures accurate resolution of the viscous sublayer in wall-bounded flows. It was observed that the $k-\epsilon$ turbulence model, a boundary layer mesh size adhering to $y^+ \leq 1$, it provided satisfactory accuracy in representing the Coanda effect for our configurations. Although further refining the choice of the most

appropriate turbulence model is possible, it is beyond the scope of this digital mirror model.

3.3.3. Boundary conditions

The boundary conditions for the digital mirror are illustrated in Fig. 6. There are three primary boundary conditions where airflow enters and exits the domain. The first boundary condition is the lateral inlet, where an average velocity is imposed. This inlet velocity ranges from 0.1 to 0.5 m s^{-1} and was initially established through a trial and error method to closely replicate the increments of electric potential in the experiments. We conducted a parametric sweep within this identified range to fine-tune the inlet velocities. In order to establish a direct relationship between the applied voltage and the inlet velocity, we traced back the velocity profiles obtained from the simulation until we found a close correspondence with the experimental data. This approach guarantees a high level of accuracy in the simulation results of the digital mirror for each specific voltage level that was tested experimentally. The second boundary condition is at the main channel inlet, where we apply 0 Pa static pressure. The same static pressure is applied at the end of the extended channel featuring flow straighteners. The remaining boundaries are either symmetry or wall, as depicted in Fig. 6.

3.3.4. Model implementation

We have implemented the physics-based CFD model using COMSOL Multiphysics version 6.1, a commercial finite element software. The turbulent CFD model is solved within a single solver study, utilizing the “Turbulent Flow, $k - \epsilon$ ” physics module in COMSOL. A parametric sweep is employed for varying the inlet velocity during simulations. An iterative segregated solver, GMRES (Generalized Minimum RESidual), is chosen in conjunction with quadratic shape functions. The solver is configured to store NaN (Not-a-Number) solutions, allowing for tracking the feasibility of inlet velocities. Furthermore, the maximum number of iterations for each sweep is 500, which was chosen based on sensitivity analysis. The computational grid is semi-automatically established with the integrated mesher tool, consisting of 454 780 mixed elements and strategic refinements in areas of interest or where significant gradients are anticipated, such as the electrode boundary. A mesh sensitivity analysis has been performed with first-order mesh element discretization, resulting in a sufficiently coarse mesh that calibrates with experimental data, reduced CPU cost, and $y^+ \approx 1$ mesh refinement.

3.3.5. Creating the digital mirror, limitations, and assumptions

We calibrate the model using experimental data by measuring the velocity profile and utilizing it as an input dataset for the validated CFD model (Rubineti et al., 2023a). This process is conducted semi-automatically, scanning a large set of inlet velocities and selecting those corresponding to specific voltages and velocity profiles. This approach enables the construction of a digital mirror to retrieve additional data, such as the amplification factor, which is challenging to extract from experimental measurements alone. The coupling between the simulation and the experiment is one-way, from the experiment to the simulation. One limitation of this digital mirror is its validity being restricted to the configuration it was trained on. Separate models need to be adjusted for each configuration, such as v1 and v2, as they yield different velocity profiles for different voltages and require distinct inlet velocities as numerical results. There is some discrepancy between experimental data and simulation results. This is expected, as we did not model the corona discharge, which introduces too high non-linearities due to high Peclet numbers in the proximity of the discharge electrode, which are difficult to converge computationally, particularly in 3D. We also did not model the sliding anemometer, which introduces a degree of blockage and a potential error margin in the experimental dataset. The assumption of an average velocity for the lateral inlet is a simplification since it is impossible to determine the velocity profile in that area without significantly disturbing the electric field in the experiments. These assumptions and limitations make the digital mirror configuration specific, but it remains valuable for complementing experimental data. Progress in ionic wind research is best achieved by combining experimental and simulation methods, given the complexity of electrostatic and fluid dynamic interactions.

3.4. Performance evaluation metrics

The operating range of the ionic wind amplifier is primarily defined by its voltage-current characteristics, which indicate the electric current flow at specific voltage levels. The operation range begins when an electric current and an airstream are detected. A Corona discharge may be measurable well before EHD air amplification takes place. Using the current-voltage ($I - U$) characteristics, the power consumption P_{el} can be easily determined with Equation (2)

$$P_{el} = UI \quad (2)$$

Another important measurement is the velocity profile, which is taken at 1-s intervals using a point-probe anemometer. From the velocity profile, the flow rate [$\text{m}^3 \text{h}^{-1}$] can be calculated using Equation (3), which is an integration of the profile:

$$\dot{V}_{out} = \sum_{i=0}^{56} w_i \cdot h_i \cdot l \quad (3)$$

In this Equation, i is an index variable representing each measurement point along a segment of the measurement line. w_i [m s^{-1}] is the airflow speed in each segment, while h_i [mm] represents the height of each segment (or the anemometer's traveling distance per second at 1.27 mm). The variable l [mm] refers to the width of the ionic amplifier unit 50 mm.

The efficiency of generating flow rates is evaluated using the transduction efficiency γ , which has the units [$\text{m}^3 \text{h}^{-1} \text{W}^{-1}$]

$$\gamma = \frac{\dot{V}_{out}}{P_{el}} \quad (4)$$

Although fan efficiency is typically described by fan pressure and flow rate curves (Onma and Chantramsi, 2018), the design of ionic wind devices focuses on generating thrust rather than pressure rise. Another way to describe efficiency is the ratio of mechanical energy to electrical energy, a commonly used metric for evaluating the efficiency of various air-moving devices. In the case of ionic wind, the efficiencies can be considerably lower when assessed using the electromechanical metric (Moreau and Touchard, 2008). More recently, efficiency improvements have been assessed using Equation (4), known as transduction efficiency. This approach, as highlighted in studies such as (Tien et al., 2020), (Wen and Ye, 2022), (Chang et al., 2020), focuses on how efficiently energy is utilized in ionic wind devices rather than merely evaluating the energy conversion rates. This distinction provides a more relevant assessment of performance for ionic wind, aligning with its operational characteristics, particularly in applications requiring localized airflow generation, such as drying (Defraeye and Martynenko, 2018).

Another efficiency metric is the amplification factor AF , which indicates the increase in flow rate achieved without additional electrical cost:

$$AF = \frac{\dot{V}_{out}}{\dot{V}_{in}} \quad (5)$$

here \dot{V}_{in} [$\text{m}^3 \text{h}^{-1}$] is the flow rate entering the wind tunnel from the side channels. This value is obtained from the CFD model by integrating the inlet velocity over the inlet area

$$\dot{V}_{in} = \int_{A_{inlet}} \mathbf{w} \cdot \mathbf{dA} \quad (6)$$

where A_{inlet} [m^2] is the inlet area. Note that \dot{V}_{in} must be multiplied by a factor of 4 to account for symmetry.

3.5. Statistical data evaluation

All anemometer measurements are replicated three times, with results reported as the average \pm standard error. Flow rate results are calculated from the average velocity measurements as detailed in Equation (3). In addition, the method of error propagation is implemented to estimate the uncertainties of the transduction efficiency γ which is a quantity derived from measurements. Equation (7) gives the propagated error of the transduction efficiency $\gamma_{prop,error}$ [$\text{m}^3 \text{h}^{-1} \text{W}^{-1}$] as

$$\gamma_{prop,error} = \frac{\dot{V}_{out}}{P_{el}} \sqrt{\left(\frac{\Delta \dot{V}_{out}}{\dot{V}_{out}}\right)^2 + \left(\frac{\Delta P_{el}}{P_{el}}\right)^2} \quad (7)$$

where $\Delta \dot{V}_{out}$ and ΔP_{el} are the standard deviations of the flow rate and the power consumption, respectively. This approach ensures a comprehensive understanding of the uncertainty in our results for transduction efficiency as a derived quantity.

We represent uncertainty using the standard error for other plots, such as those showing airflow velocity, flow rate and power consumption. This is because these plots are based on direct measurements, where standard error effectively captures the variability and precision of the data. The standard error is represented as an error bar for each average. All statistical analyses are conducted using R (RStudio | Open source).

4. Results

In this section, we present the findings of our study by analyzing the impact of various design parameters on the performance of the ionic wind amplifier. We begin by examining the effect of the distance between the emitter and rod collector electrodes on velocity profiles and performance metrics. Next, we compare the performance of plate and rod collectors, then assess the impact of adding multiple stages on airflow and pressure rise. We then analyze the performance of diverging walls in the air amplifier compared to straight walls. Finally, we discuss the digital mirror and the design's implications for using fewer needles.

4.1. Distance between emitter and rod collector electrodes

4.1.1. Velocity profiles

Fig. 7 presents the velocity profiles for the rod collector configuration with two different interelectrode distances of $\delta = 20$ mm and 30 mm. It is observed that a shorter interelectrode distance results in a narrower possible operational range for the voltage, spanning from 10

kV to a maximum of 18 kV. On the other hand, a longer interelectrode distance allows for a broader voltage range, up to 25 kV, and results in a higher speed. However, this comes with larger velocity fluctuations and a larger standard deviation from the average.

In configuration v2, electrical breakdown occurs directly after 25 kV, leading to unstable current and discharge, translating into substantial airspeed variations. A similar pattern is observed for the 30 mm distance at 10 kV, where the lower threshold of discharge formation causes significant fluctuations in airspeed. This analysis highlights the influence of interelectrode distance on the operational range and stability of the ionic wind amplifier and its impact on airspeed variations.

The ideal scenario has an inter-electrode distance of 30 mm and operates within a 15–20 kV voltage range. This selection is based on the observed lower airspeed variability and relatively higher airspeed within the amplification region ($h = 10$ mm–60 mm). Within the area of amplification, increasing the voltage beyond this range does not result in a proportional increase in momentum. Instead, higher voltages predominantly increase airspeed at the velocity profile's peaks.

4.1.2. Performance metrics

The performance metrics of airflow rate, power consumption, and transduction efficiency for the v2 rod configuration at two inter-electrode distances in Fig. 8 reveal that a shorter inter-electrode distance consistently generates a higher flow rate. For instance, at the benchmark voltage of 15 kV, the flow rate is approximately 32 % higher for the 20 mm distance ($5.3 \text{ m}^3 \text{ h}^{-1}$) compared to the 30 mm distance ($4 \text{ m}^3 \text{ h}^{-1}$). However, the power consumption for the 20 mm distance is over

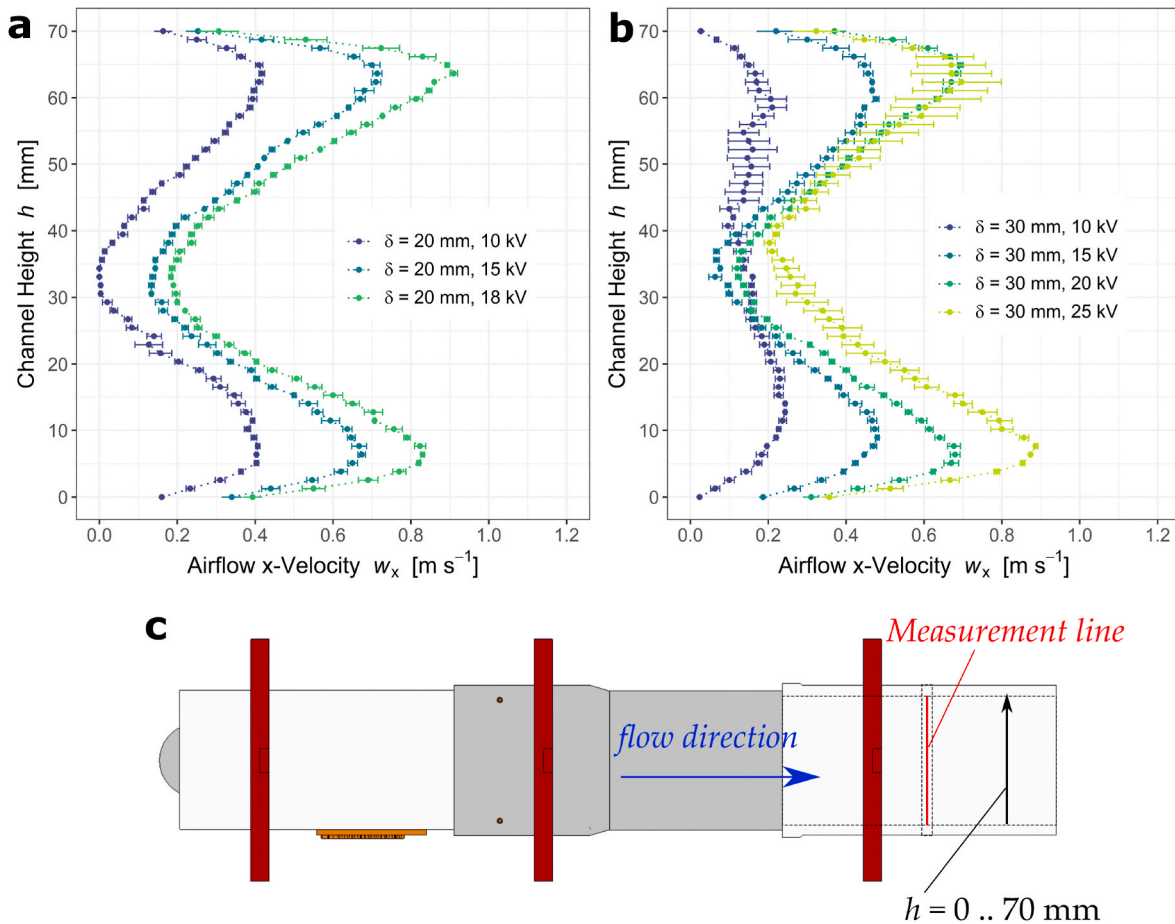


Fig. 7. Velocity profiles for the rod collector configuration with two different interelectrode distances $\delta = 20$ mm (a) and 30 mm (b). A shorter distance provides a shorter operation range from 10 kV to a maximum of 18 kV. A long-distance allows up to 25 kV electric potential, albeit with a more considerable error margin. In v2, breakdown occurs immediately after 25 kV, causing current and discharge instability and more significant airspeed variations. Similarly, for a 30 mm distance at 10 kV, the lower threshold of discharge formation results in significant airspeed fluctuations.

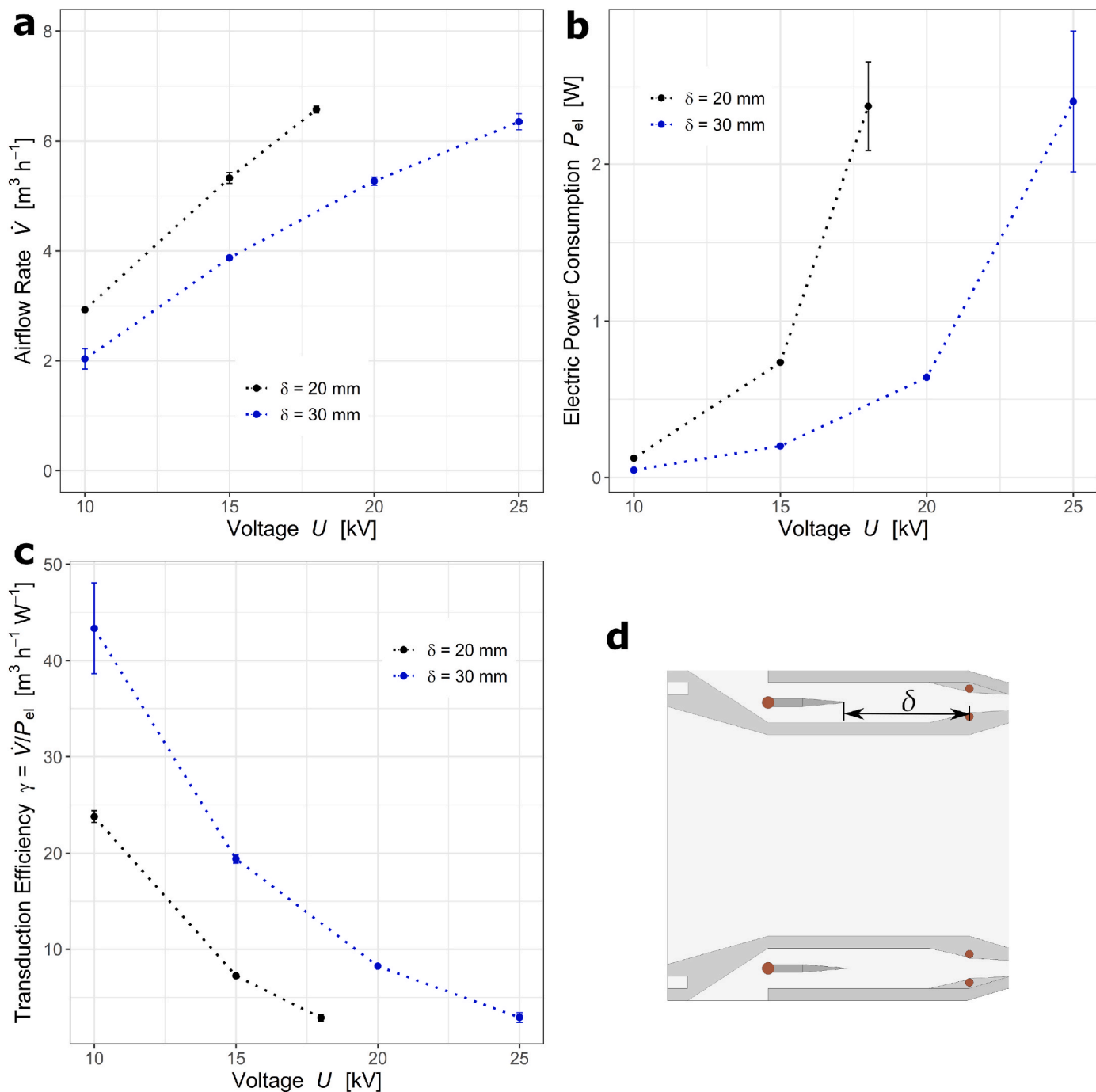


Fig. 8. Experimental performance metrics of airflow rate (a), power consumption (b), and transduction efficiency (c) for the v2 rod configuration at two inter-electrode distances. The experimental data show that a shorter needle consistently produces more flow rate. At the 15 kV benchmark voltage, it is approximately 32.5% higher ($5.3 \text{ m}^3 \text{h}^{-1}$ for 20 mm compared to $4 \text{ m}^3 \text{h}^{-1}$ for 30 mm) but at a higher electrical cost, with power consumption being more than twice as high (0.7 W for 20 mm and 0.22 W for 30 mm). This makes the shorter distance, not the most efficient choice based on the measured data.

twice as high (0.7 W) compared to the 30 mm distance (0.22 W), rendering the shorter distance less efficient. Our tests demonstrate that a longer inter-electrode distance facilitates the efficient generation of the ionic wind jet and, consequently, a more considerable momentum exchange volume in the side channels for the ionized air (Ramadhan et al., 2017b). A 30 mm inter-electrode gap allows for a more stable operating range between 15 and 20 kV.

4.2. Performance of a plate collector vs. rod collector

4.2.1. Velocity profile

Fig. 9 presents the plate collector configuration v1 velocity profile across various voltage levels. A notable observation is the asymmetric velocity profile at 10 kV. The lower side channel ($h = 0-10$ mm) produces a more vigorous discharge than the upper side ($h = 60-70$ mm), which could be due to manufacturing impurities. This asymmetry is also evident at higher voltage levels, although to a lesser extent. Notably, the plate collector configuration increases the voltage to 30 kV, providing a broader operational range. The implications of these findings on the

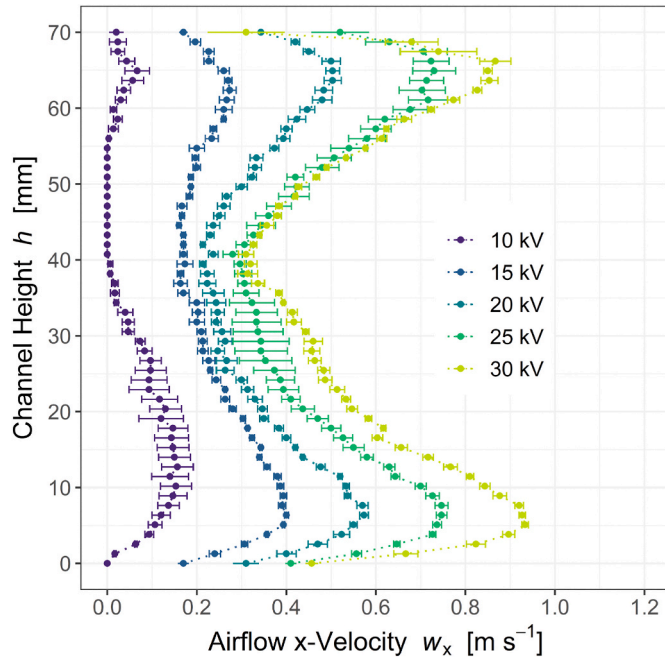


Fig. 9. Experimental velocity profile across voltage levels for the plate collector configuration v1. At 10 kV, the measurements indicate a notably asymmetric velocity profile, with the lower side channel ($h = 0\text{--}10\text{ mm}$) generating a more potent discharge than the upper side channel ($h = 60\text{--}70\text{ mm}$). Beyond 10 kV, the asymmetric trend persists, although less pronounced. Furthermore, the voltage can be increased up to 30 kV as observed in our experiments.

overall performance of the plate collector configuration will be further discussed in the subsequent sections (see Fig. 10).

4.2.2. Velocity profile comparison

In Error! Reference source not found., we compare the velocity profiles for the plate collector v1 and rod collector v2 configurations at 15, 20, and 25 kV, with an inter-electrode distance of 30 mm. The rod collector consistently displays higher peak velocities and slightly lower velocities in the amplification zone. However, at 25 kV, the profiles become similar.

Overall, the similar flow rate performance of both configurations can be attributed to the differences in how the airspeed is dispersed along the ionic wind amplifier height. While the plate collector v1 has lower peak velocities but exhibits higher speeds in the middle section. In contrast, the rod collector v2 accelerates more in the wall region.

4.2.3. Performance metrics

Fig. 11 compares airflow rate, power consumption, and transduction efficiency performance metrics for the v1 plate configuration with the v2 rod configuration at an inter-electrode distance of 30 mm. The rod configuration shows a slightly higher airflow rate, while the plate configuration offers a more extensive operation range. Power consumption is quite similar, up to 20 kV. Interestingly, at 25 kV, both configurations produce the same flow rate. However, the rod configuration consumes more than twice as much electrical power. We suspect that this deviation at 25 kV is due to the reduced exposed surface area of the rod collector. At higher voltages, more charges accumulate on the dielectric material (PA-GF) because of less contact between the ion cloud and the collector (Iranshahi et al., 2020).

Consequently, a micro-environment with a higher average electric field is created in the side channel, which promotes spark formation sooner, as observed in the case of v2. However, both configurations perform well in our preferred voltage range of 15–20 kV, offering an acceptable trade-off between airflow rate, power consumption, and transduction efficiency.

4.3. Impact of adding multiple air-amplifier stages on the airflow and pressure rise

4.3.1. Performance metrics

In Fig. 12, we compare the performance metrics for the v2 rod configuration with one, two, and three stages, including airflow rate, power consumption, and transduction efficiency. It is observed that adding a second stage can increase the flow rate by up to 50% at 20 kV. In contrast, the power consumption increases from 0.4 to 0.6 W. Introducing a third stage results in only marginal improvements in flow rate and power consumption. Adding multiple stages does not result in a proportional increase in airflow rate.

4.3.2. Velocity profile and pressure rise comparison

Fig. 13 compares the velocity profiles for single-stage and multistage configurations at the preferred voltages of 15 and 20 kV. The most notable difference is that multiple stages enhance the velocity in the amplification section. Additionally, peak velocities also increase, although to a lesser extent.

To evaluate the influence of many stages on system pressure, we would ideally quantify the static pressure rise, which is often the central issue in ventilation and airflow systems and is typically reported as a fan performance metric. However, we concentrate on dynamic pressure due to the difficulties in reliably detecting static pressure in our experimental setup. Although dynamic pressure does not precisely correspond to static pressure, it can provide insight into pressure changes within the system by acting as a scaled measure of velocity. To quantify the impact of multiple stages on the dynamic pressure, we employ Equation (7) for dynamic pressure:

$$p_{dyn} = \frac{1}{2} \rho \bar{w}_x^2 \quad (8)$$

where p_{dyn} [Pa] represents the dynamic pressure, ρ is the air density 1.2 kg m^{-3} , and \bar{w}_x [m s^{-1}] denotes the mean horizontal velocity component. Using this Equation, we can compute the dynamic pressure changes and increments for different configurations.

Table 2 compares dynamic pressure changes and increments for the preferred voltages of 15 and 20 kV across one, two, and three-stage configurations. The data demonstrates that adding multiple stages results in a more actual airspeed, further contributing to the improved velocity profiles observed in multistage setups. This improvement is particularly evident in forming a block profile flow within the amplification section, which could be advantageous for specific applications requiring uniform and stable flow characteristics. However, quantifying dynamic pressure also highlights that ionic wind amplifiers exhibit limitations in overcoming significant pressure resistance compared to conventional fans. As such, ionic wind devices are more suitable for air distribution and localized airflow generation where a modest pressure rise is sufficient.

4.4. Performance of diverging vs. straight coanda surface

4.4.1. Velocity profile

Fig. 14 presents the velocity profile across different voltage levels for the rod collector configuration v2, equipped with a convex Coanda surface with a broad cross-section of $100\text{ mm} \times 50\text{ mm}$. For this experiment, the voltage was increased in 2.5 kV steps because we saw a sharp, almost zero-decay of the velocity in the amplification zone. However, across all voltage levels, we see the same behavior, and while the peak velocities increase with voltage, the velocity profile at the midline of the channel remains almost constant ($<0.2\text{ m s}^{-1}$). While the Coanda effect is present with the convex shape, the expected air entrainment is not detected. We observe some amplification, i.e., a measurable airstream at $h = 50\text{ mm}$ with the highest voltage setting.

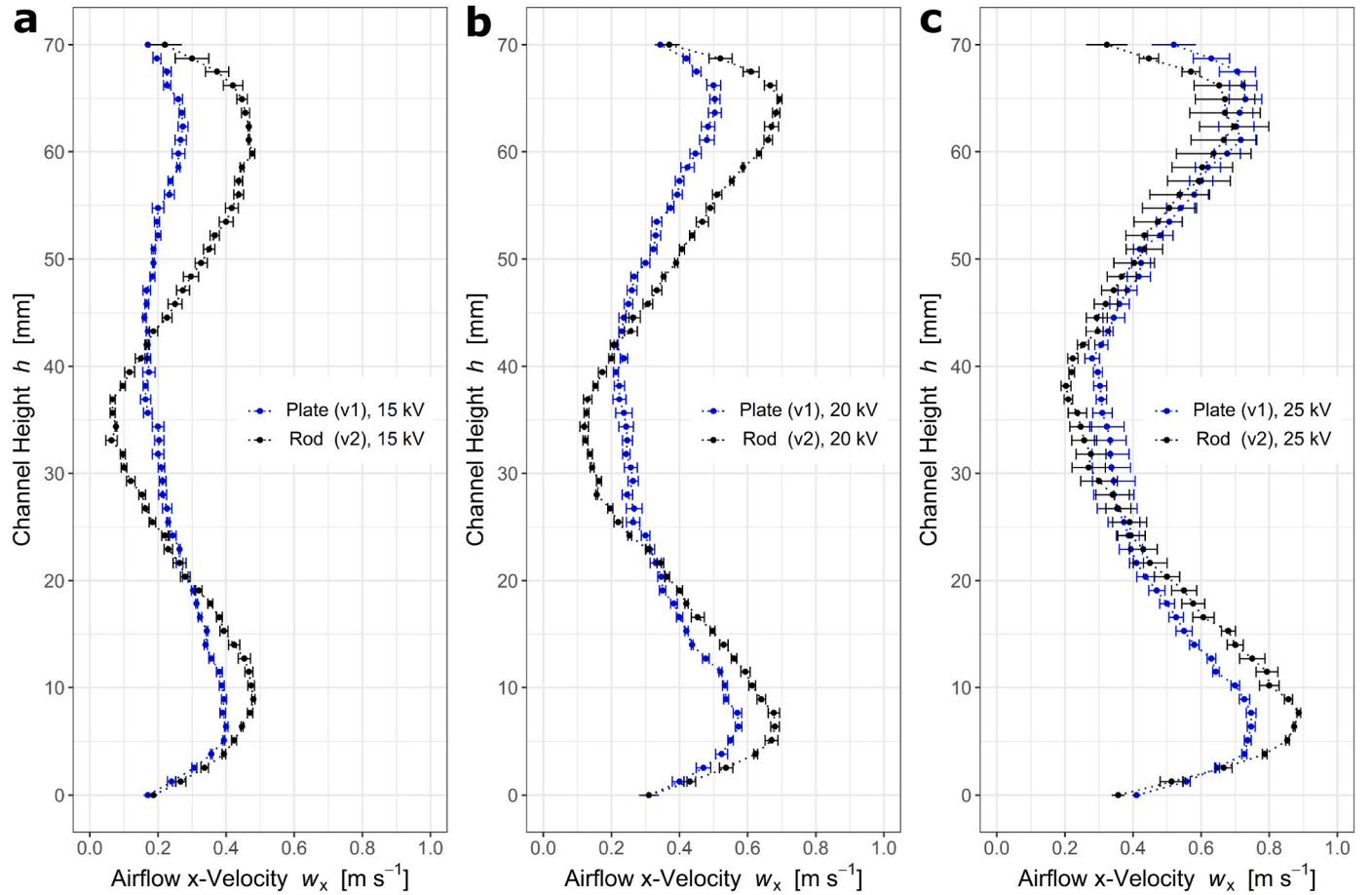


Fig. 10. Experimental comparison of velocity profiles for the plate collector (v1) and rod collector (v2) configurations at 15 (a), 20 (b), and 25 kV (c) with an inter-electrode distance of 30 mm. From the experimental results, it is observed that the rod collector exhibits consistently higher and slightly lower peaks in the amplification zone. At 25 kV, the profiles appear to be quite similar, taking into account the error margin.

4.4.2. Performance metrics

Fig. 15 illustrates the performance metrics (airflow rate, power consumption, and transduction efficiency) for the v2 rod configuration equipped with a wide configuration featuring a convex Coanda surface. While the velocity profile exhibits a sharp decay in velocity in the middle section, the wide configuration still delivers slightly higher flow rates overall. As expected, the power consumption remains unchanged, as with the rod collector, since the core part is unchanged. However, due to the finer increments of 2.5 kV, we observe that the increase in power consumption from 20 to 22.5 kV is less pronounced than from 20 to 25 kV. This observation suggests that a reasonable operational range for the v2 configuration could be extended to approximately 22.5 kV. This information may prove helpful in further refining the design and optimizing the performance of ionic wind amplifiers equipped with convex Coanda surfaces.

4.4.3. Velocity profile comparison

In Fig. 16, we compare the velocity profiles between the wide and regular configurations for 15, 20, and 25 kV. The y-axis representing the height of the channel is normalized for direct comparison between configurations. Both profiles share a similar shape; however, the wide configuration tends to exhibit lower velocities in the middle section. This comparison demonstrates that divergent barriers do not necessarily improve flow profile uniformity. A consistent and narrow channel height produces a more homogenous flow profile with greater velocities across the amplification zone.

4.5. Digital mirror results

In this section, we present the digital mirror model, a combined experimental and numerical approach, to analyze the performance of the ionic wind amplifier. The combination of numerical and experimental methods is crucial for ionic wind-related engineering, as the complexity of the problem makes stand-alone methods less effective for conducting thorough investigations.

Fig. 17 displays a post-processed simulation result of the flow field and streamlines in 3D for half of the ionic wind amplifier channel. The streamlines are predominantly straight, indicating a swirl-free flow within the system. This visualization offers valuable insights into the behavior of the ionic wind amplifier under various operating conditions.

Table 3 compares the outlet flow rate results obtained from the experiments and the simulation. The agreement between the experimental and simulated data showcases the reliability and accuracy of the digital mirror model in predicting the performance of the ionic wind amplifier. The plate collector configuration v1 shows a significant discrepancy between experimental and numerical results at 192 % in only one case. This deviation is explained because the configuration produces quite an asymmetric and weak flow at 10 kV, as seen in Fig. 9. In this case, we consider the simulation result to be more accurate. The remaining configuration and voltages are within commonly accepted error margins in CFD workflow (Versteeg and Malalasekera, 2007). The remaining deviations can be explained in detail with the velocity profile comparison in Fig. 18. While there is some deviation in the results at lower voltage levels, the 20 and 25 kV profiles show a strong alignment between simulation and experiment. These observations could be due to

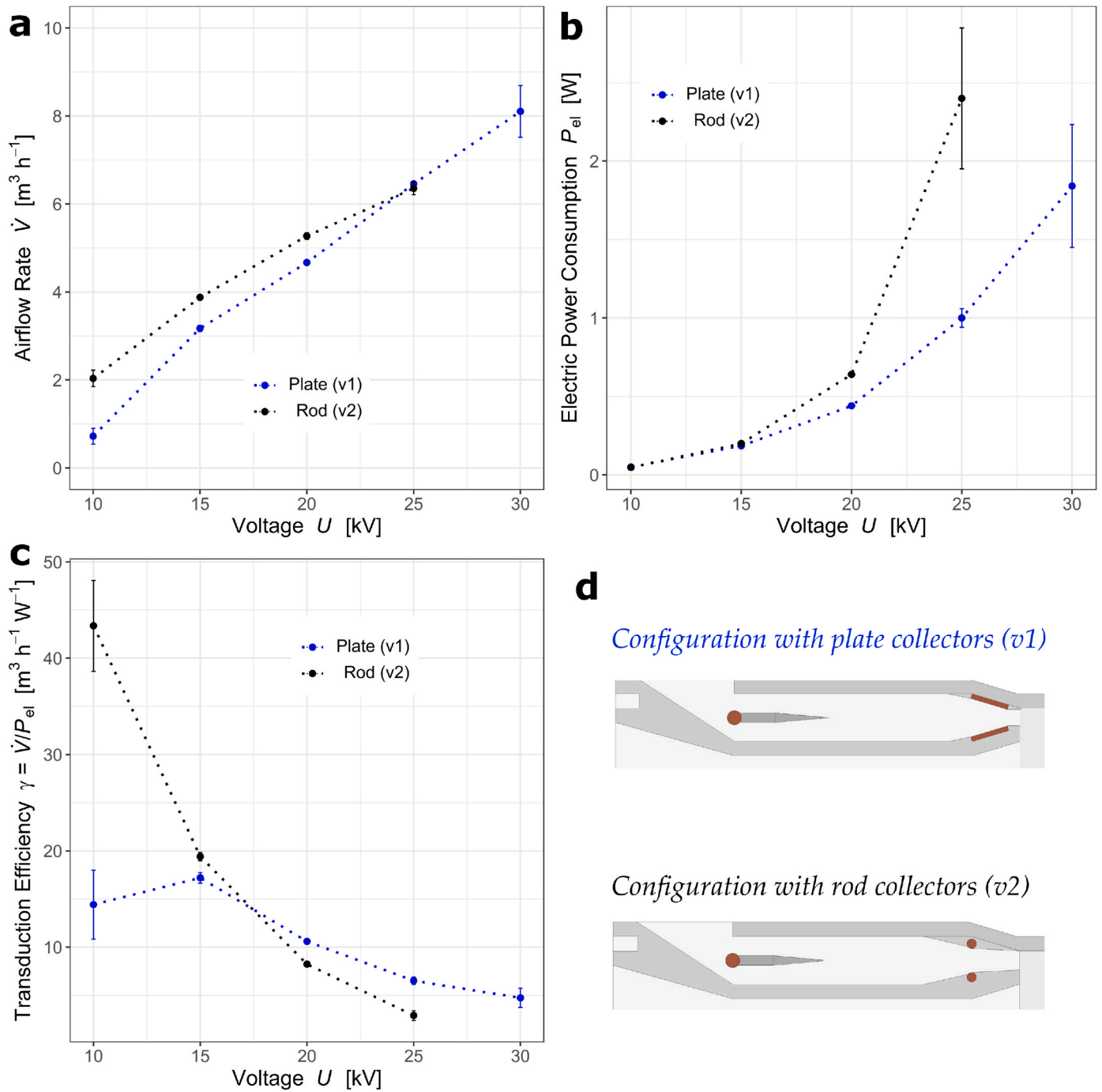


Fig. 11. Comparison of performance metrics (airflow rate (a), power consumption (b), and transduction efficiency (c)) for the v1 plate and v2 rod configurations at an inter-electrode distance of 30 mm. The rod configuration exhibits a marginally higher airflow rate, while the plate configuration benefits from a broader operating range. Power consumption remains similar up to 20 kV; however, at 25 kV, both configurations achieve the same flow rate, but the rod configuration consumes over twice the electrical power. Both collector designs perform comparably well in the preferred range of 15–20 kV.

turbulence modeling. Overall, the digital mirror model provides good predictions for the ionic wind amplifier's performance.

Fig. 19 exhibits the amplification factors derived from the digital mirror model and is not easily measurable with anemometers. The amplification factor is an efficiency metric that indicates the increase in flow rate obtained per unit of electrical cost. The model predicts amplification factors ranging from 2.6 to 3.3 for the studied voltage range.

In addition to the previously discussed digital mirror results, we have identified a notable relationship between the adjusted inlet velocity derived from the simulation and the square root of the electric current in

our ionic wind amplifier. This relationship is illustrated in Fig. 20 and shows two distinct linear trends. In the lower current range, up to $5.7 \sqrt{\mu A}$, we observe a steeper increase in inlet velocity, suggesting that the device operates more efficiently. This regime effectively converts more of the electrical input into airflow. Beyond $5.7 \sqrt{\mu A}$, the trend shifts to a flatter slope, indicating that the additional electric current does not produce the same proportional increase in airflow velocity. The observed behavior can be explained by the higher rate of charge dissipation, which is likely due to charge saturation occurring in the side channels (Sigmond, 1982). This phenomenon impedes the efficient

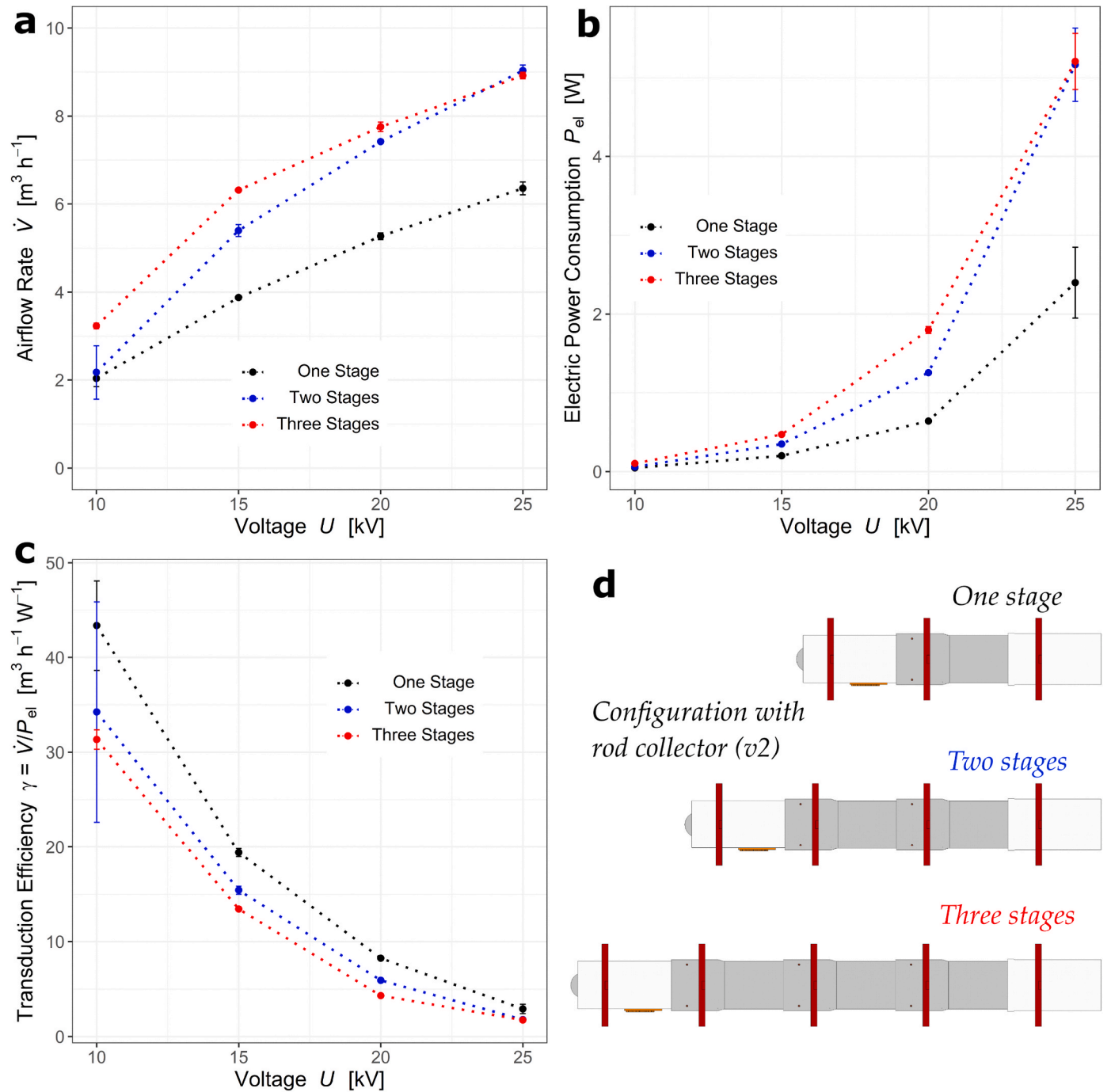


Fig. 12. Performance metrics (airflow rate (a), power consumption (b), and transduction efficiency (c)) for the v2 rod configuration with one, two, and three stages compared. Adding a second stage can increase the flow rate by up to 50 % at 20 kV, with the power consumption rising from 0.4 to 0.6 W. The third stage provides marginal improvements in flow rate and power consumption. Adding multiple stages does not double the airflow or current, which is anticipated, as all needles are connected in series to the same high-voltage power supply, leading to current distribution.

conversion of produced charge into directed airflow. These observations highlight the intricate nature of electrohydrodynamic phenomena that propel the ionic wind amplifier. They also illustrate the necessity of addressing improvements in ionic wind technology using a combination of numerical and experimental approaches.

4.6. Impact of reducing the number of needles

Here, we explore the impact of reducing the number of needles on the performance of the ionic wind amplifier. Fig. 21 presents the performance metrics (airflow rate, power consumption, and transduction

efficiency) as a function of voltage for different numbers of needles (4, 2, and 1) on each side of the ionic wind amplifier. The airflow rate curves shift nearly linearly across the voltage range when the number of needles is reduced. Interestingly, the power consumption is not significantly affected by the number of needles below 20 kV. This observation could be attributed to the separation distance of 10 mm between needles in the original (four-needle) configuration. Below 20 kV, the charge generation appears to spread evenly across the needles with little interaction. At higher voltage levels, the ionic wind amplifier profits from fewer needles as more charges can be more evenly spread spatially. As a result, it is possible to attain higher voltage levels beyond 25 kV as charge

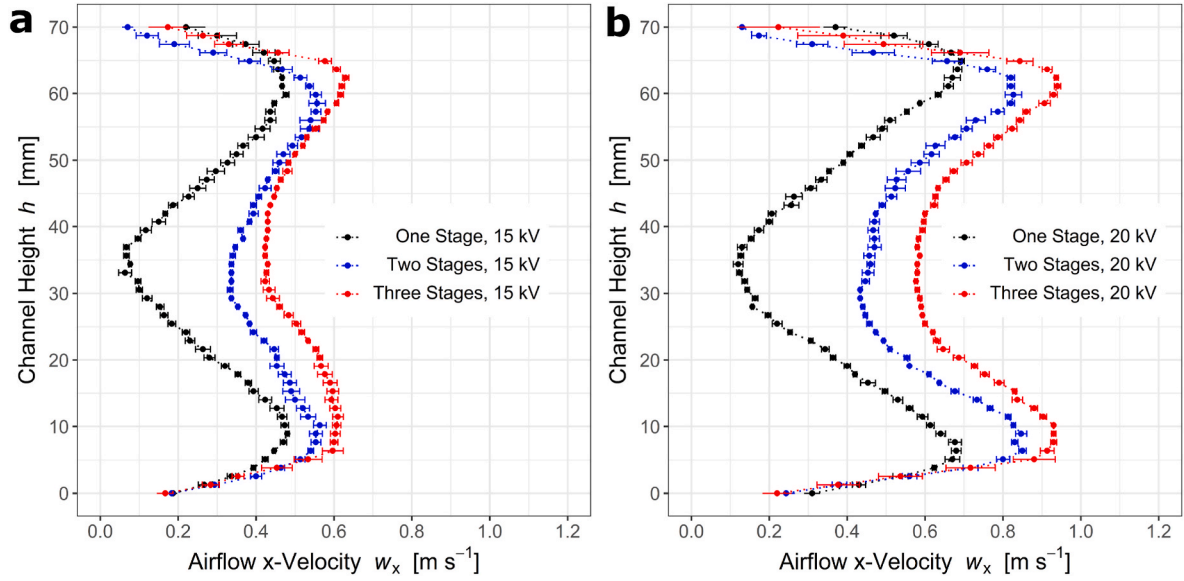


Fig. 13. Comparison of velocity profiles for the preferred voltages of 15 (a) and 20 kV (b) for single-stage and multistage configurations. The most notable difference is that multiple stages enhance the velocity and formation of a block profile flow in the amplification section. Peak velocities also increase, albeit to a lesser extent.

Table 2

Comparison of dynamic pressure changes and increments for the preferred voltages of 15 and 20 kV across one, two, and three-stage configurations.

No. Of stages	Voltage	Power consumption	Average velocity	Dynamic pressure	Increase compared to reference
	U [kV]	P_{el} [W]	\bar{w}_x [m s^{-1}]	p_{dyn} [Pa]	[%]
1	15	0.2	0.3	0.054	n/a (reference for 15 kV)
1	20	0.64	0.4	0.096	n/a (reference for 20 kV)
2	15	0.35	0.43	0.111	205 %
2	20	1.25	0.59	0.209	217 %
3	15	0.47	0.49	0.144	266 %
3	20	1.8	0.7	0.29	302 %

saturation occurs later with fewer needles. Between 10 and 15 kV, the four-needle configuration is observed to be the most efficient. In contrast, at 20 kV, the efficiencies of all configurations are roughly equivalent. The effect of reducing the number of needles reveals that an extruded air amplifier with fewer needles could produce marginally lower flow rates.

5. Discussion

In this study, we have experimentally and numerically investigated several design aspects of the first ionic wind amplifier prototype. This study serves as a starting point for further refinements of the design. The design is compact and scalable.

An important finding from our investigation was that an inter-electrode distance of 30 mm provides an optimal equilibrium between stability and performance. This result supports the observation that, at higher voltages, ionization processes lose more electrical energy without transferring proportionally more momentum to the air.

One of the more notable findings of our study involves the emitter-collector configurations. The emitter-collector configuration has always been an active area of research and improvement for electrohydrodynamic-driven airflows (Zhang and Lai, 2011). In our experiments, the v2 rod configuration slightly outperforms the plate collector configurations regarding airflow rate and efficiency, confirming the importance of optimizing the collector design to achieve better

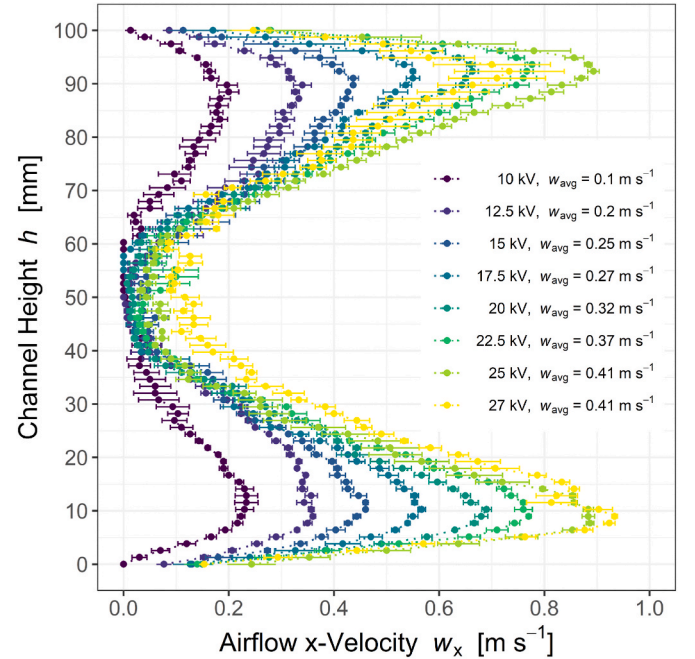


Fig. 14. Velocity profile across voltage levels for the rod collector configuration v2 with a convex Coanda surface featuring a cross-section of 100 mm × 50 mm. Voltage increments were selected in 2.5 kV steps due to the sharp, near-zero velocity decay observed within the amplification zone. Similar behavior is exhibited regardless of the voltage level, with peak velocities increasing as voltage rises. At the same time, the middle section of the wind tunnel remains nearly stagnant.

performance. However, the v1 configuration with plates yields a more extensive voltage operation window. This finding that a greater inter-electrode distance improves performance is somewhat counterintuitive, as it is commonly observed that ionic wind devices without amplification mechanisms are more effective with shorter distances.

Nonetheless, the advantages of a greater distance become evident when the combined effects of the channel shape and ionic wind operating parameters are considered. This indicates a complex interaction

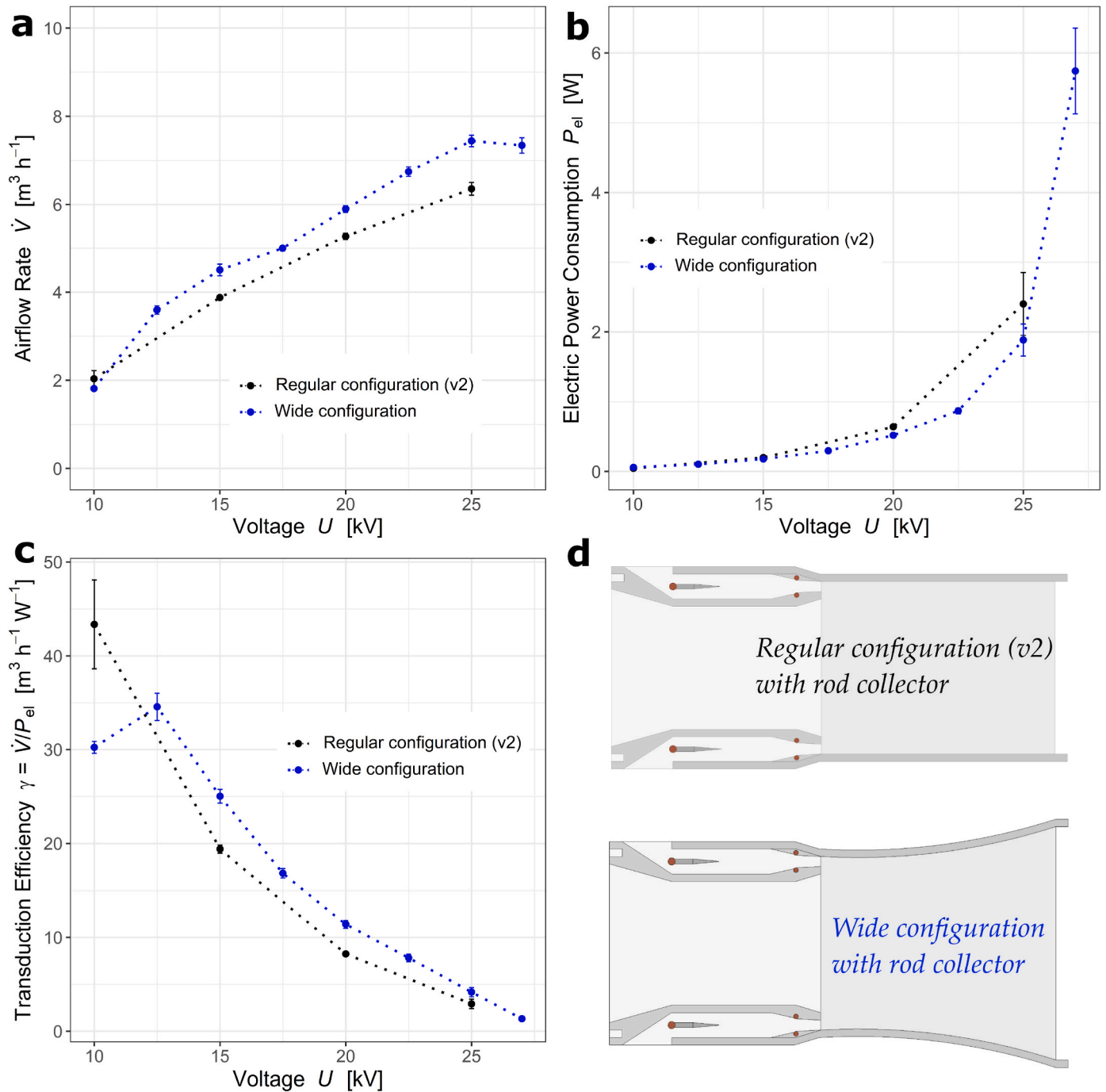


Fig. 15. Performance metrics (airflow rate (a), power consumption (b), and transduction efficiency(c)) for the v2 rod configuration equipped with the wide configuration featuring a convex Coanda surface. Despite the sharp decay in velocity observed in the middle section of the velocity profile, the wide configuration still delivers slightly higher flow rates. This effect is presumably driven simply by the larger surface area.

between geometric and electrohydrodynamic parameters, establishing the groundwork for further future research to optimize the ionic wind amplifier. In the side channel of the v2 configuration, a microenvironment with a higher average electric field is created, which accelerates the formation of sparks. Overall, both configurations are equally helpful for low-power airflow generation. It is also worth noting that in this study, the rod's exposed surface area was a fraction of the plate collector's surface area. We speculate that a larger rod collector diameter might have obtained a different outcome. This highlights the vast design space of the EHD system, suggesting that future work should explore this space more widely.

Regarding the number of stages, our results indicate that while

adding more sequential stages can increase the flow rate by 50 %, it generally does not significantly affect overall performance. Given that all needles are connected in series to the same high-voltage power supply, resulting in the current being distributed among the stages, this result is somewhat predictable. This observation highlights the law of diminishing returns when adding more stages to a system, providing valuable insights for future design decisions and optimizations of multistage ionic wind amplifiers. A more effective approach might be to use the ionic wind amplifier parallel or in an array, focusing on optimizing individual stages. In array formation, another point of improvement could be to remove the inner walls to make a larger ionic wind amplifier.

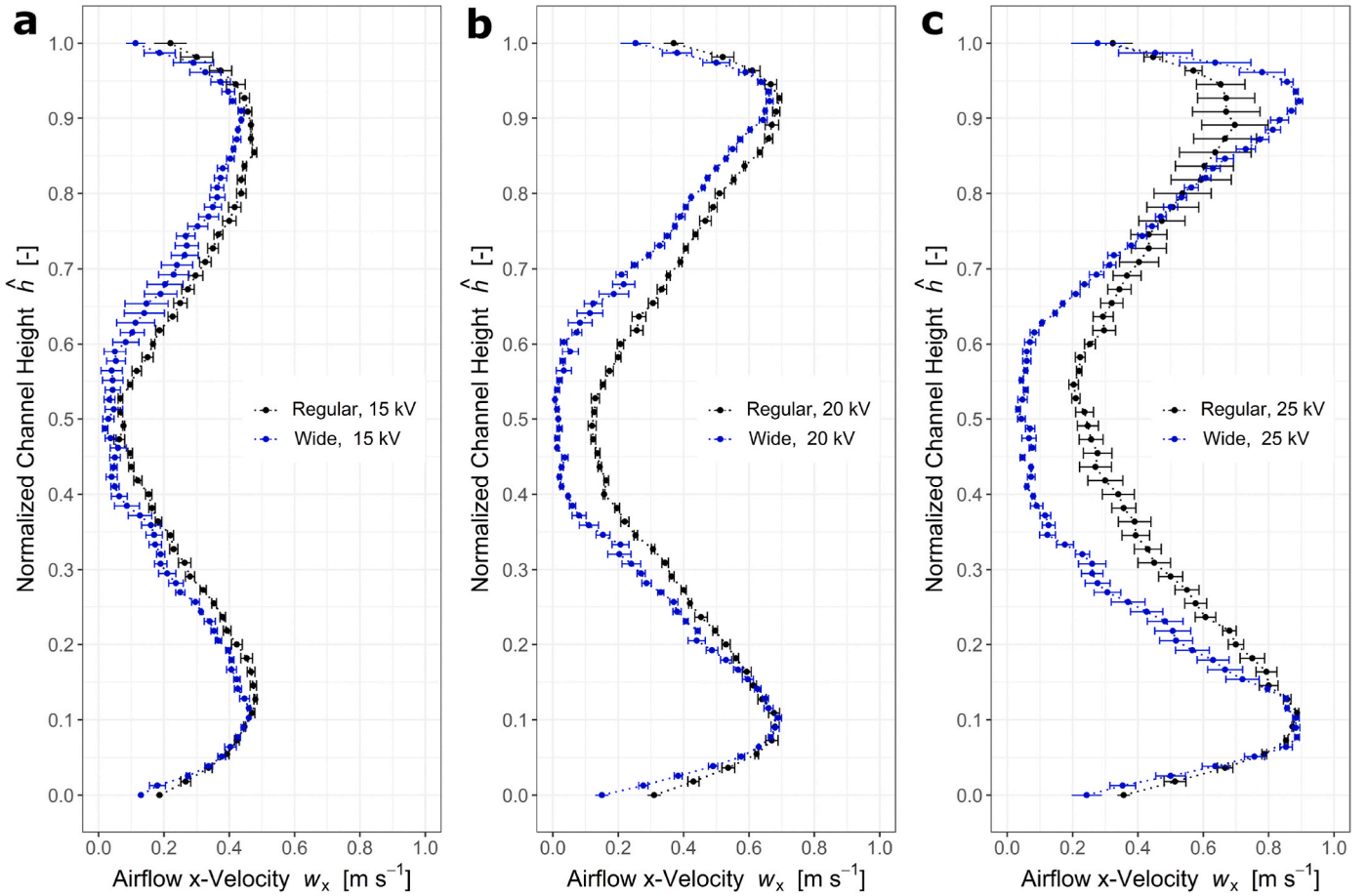


Fig. 16. Velocity profile comparison between the wide and regular configurations for 15 (a), 20 (b), and 25 kV (c) with a normalized y-axis representing the height of the channel. While both profiles share a similar shape, the wide configuration tends to exhibit lower velocities in the middle section. This comparison provides valuable insights into the dynamics of the Coanda effect within the ionic wind amplifier. Contrary to initial expectations, divergent walls do not necessarily enhance the amplifier's performance.

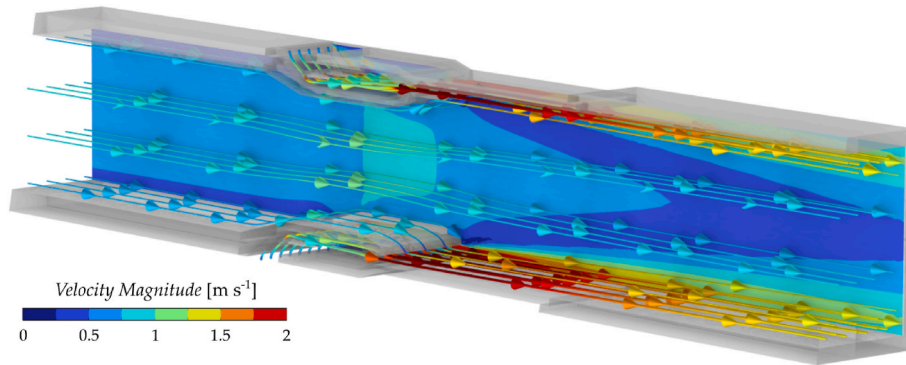


Fig. 17. Simulation results illustrating the flow field and streamlines within half of the ionic wind amplifier channel. The visualization highlights the predominantly straight nature of the streamlines, suggesting a swirl-free airflow within the device.

One of the most intriguing results of our investigation is the comparison between convex and straight Coanda surfaces. It revealed that divergent walls drew more air into the ionic wind amplifier, even when the inner velocity was reduced to zero in the center of the arrangement. We did not detect the expected air entrainment with the convex Coanda surface, which is a perplexing observation. Possibly this outcome can be attributed to the simultaneous implementation of a diverging form and increased cross-section. The discovery suggests that while leveraging the Coanda effect for ionic-wind-driven flows is feasible, a more substantial downstream velocity is required for increased air entrainment. This

hypothesis is supported by increased amplification at higher voltage settings in the straight Coanda surface arrangement. Future research and experiments are required to acquire a deeper understanding of this phenomenon and identify the most effective techniques for optimizing the performance of ionic wind amplifiers with a convex Coanda surface. Divergence tends to be more effective when dealing with higher-velocity flows, provided they are not too low to cause separation or increase viscous dissipation. With a current peak velocity of up to 1 m s^{-1} , maintaining a straight Coanda surface and a narrow channel appears more effective in inducing an airflow in the center of the device.

Table 3

Comparison of outlet flow rate results between the experimental data and the simulation, demonstrating the accuracy of the simulation model in replicating the performance of the ionic wind amplifier for voltages 10–25 kV in both configurations.

Configuration	Voltage [kV]	Outlet flow rate [$\text{m}^3 \text{h}^{-1}$]		Error [%]
		Experiment	Simulation	
Plate collector (v1)	10	0.73	2.15	192
	15	3.15	3.38	7.0
	20	4.6	4.63	0.7
	25	6.33	5.9	−6.8
Rod collector (v2)	10	2.04	2.07	1.6
	15	3.88	4.4	13.4
	20	5.27	5.57	5.7
	25	6.36	6.75	6.3

The digital mirror model analysis purposefully predicts the performance of the ionic wind amplifier. It emphasizes the importance of combining numerical and experimental methods for ionic wind-related engineering. The model assists our experimental work by providing additional data that is otherwise difficult to obtain, like the inlet flow rate from the side channels of the prototype. While the current digital mirror is invaluable in extending our experimental insights, we envision it to evolve into a more comprehensive digital twin. In this enhanced version, the model would further integrate electrostatics, enabling us to utilize the experimental dataset for validation instead of calibration. This advancement would improve the model's accuracy and predictive capability, enabling an even more holistic understanding of the ionic wind amplifier phenomena.

A result that initially seems unexpected is that we discovered that the number of needles used had little impact on the airflow rate. However, it is consistent with studies showing that too little or too much space between needles reduces the impact of needle amount (Bashkir and Martynenko, 2021). Our observation aligns with previous findings highlighting a significant interaction between channel geometry, needle spacing, and the needle number's impact on device performance. In

certain instances, fewer needles may result in more cost-effective designs without severely affecting flow performance. These results could direct future research to investigate the 'needle count threshold,' beyond which there is no further increase in airflow rate, paving the way for optimized needle configurations that prevent unnecessary needle density. The ionization zones of extra needles in our compact design will likely overlap, reducing the effect of altering needle counts.

We still need to study the degradation of the needles over extended periods of use. Some research on tungsten wires suggests that after 450 h, the surface becomes quite corroded (Cogollo de Cádiz et al., 2021). While testing our prototype, we experimented with several wire electrodes as an alternative. We found that wire electrodes were unsuccessful, resulting in sparkover rather than a stable discharge. This experience highlights the significance of the emitter's geometry in effectively producing ionic wind in a limited space. Tungsten was selected as the needle material due to its high resistance to corrosion and strong mechanical stability. While the basic principles of our research can be extended to other conductive materials such as copper or stainless steel, it is crucial to acknowledge that each material has unique manufacturing difficulties. The material's ability to be finely ground into the precise needle shape is critical for functionality. Based on our experience, we have found that although various materials may be theoretically possible. Nonetheless, the practical aspects of producing and maintaining the sharpness and durability of the emitter are crucial considerations in deciding which material to use.

This extensive study has investigated a prototype with a technology readiness level that can be translated into commercial products for sustainable and low-power air propulsion. In general, ionic wind amplifiers are suitable as retrofit solutions for larger systems that need tailored airflow distribution with slight pressure rise. Moreover, as Corona discharge is a non-thermal plasma, it generates airflow without additional heat due to mechanical friction. We recommend implementing this technology first in controlled industrial settings rather than domestic environments, as ozone production has not been quantified and is still an open research point.

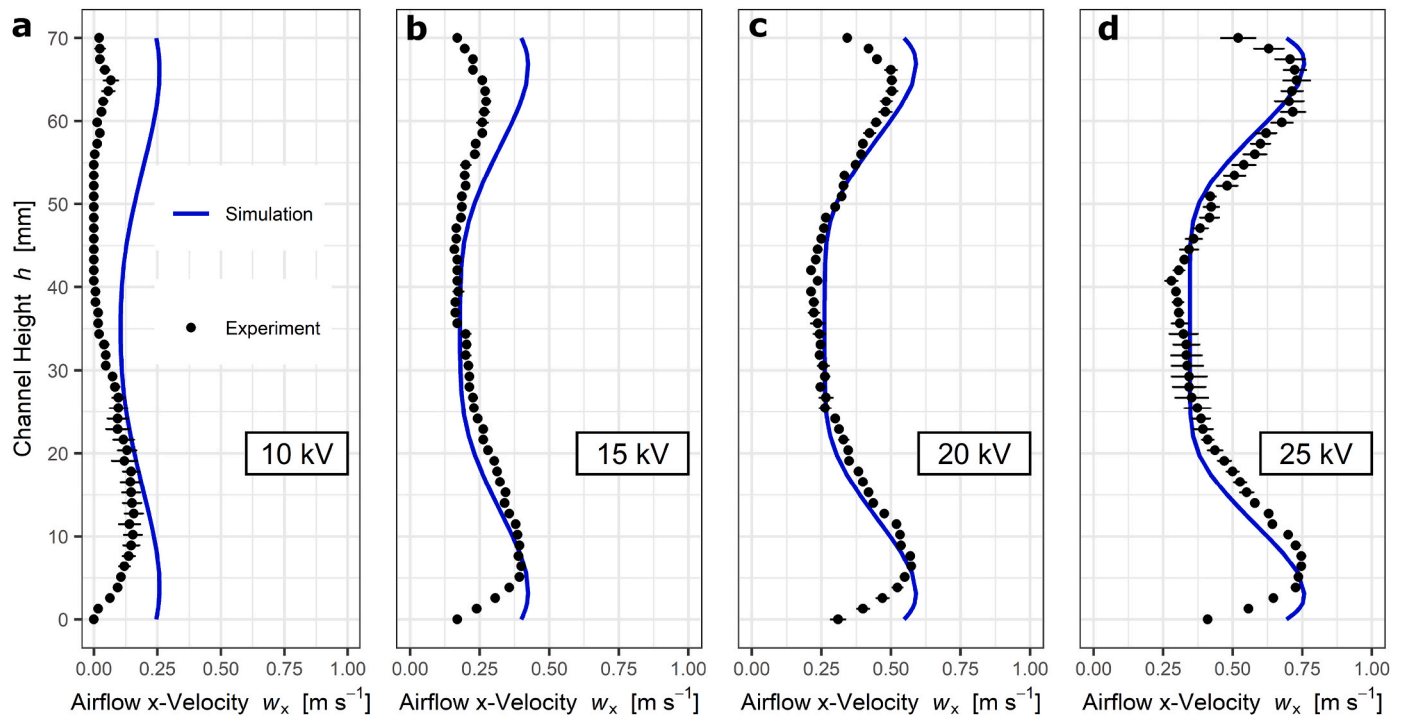


Fig. 18. Comparison of velocity profiles between the experimental data and the simulation for voltage levels of 10 (a), 15 (b), 20 (c), and 25 kV (d). The results show a satisfactory agreement between the two data sets, particularly at 20 and 25 kV. The deviations observed at lower voltage levels may be attributed to experimental factors or the need for further simulation fine-tuning. Overall, the consistency demonstrates the reliability of the digital mirror.

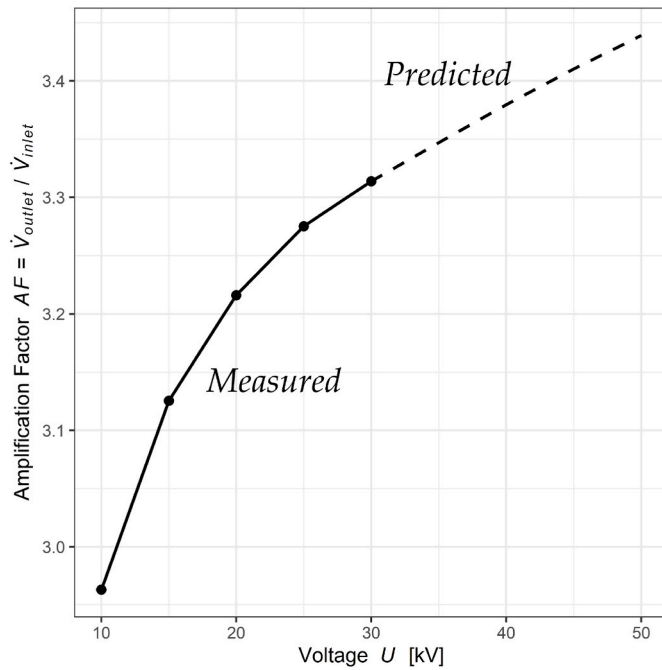


Fig. 19. Amplification factor derived from the digital mirror model, showcasing the efficiency of the ionic wind amplifier across various voltage levels. The model predicts amplification factors ranging from 2.6 to 3.3 for the studied voltage range.

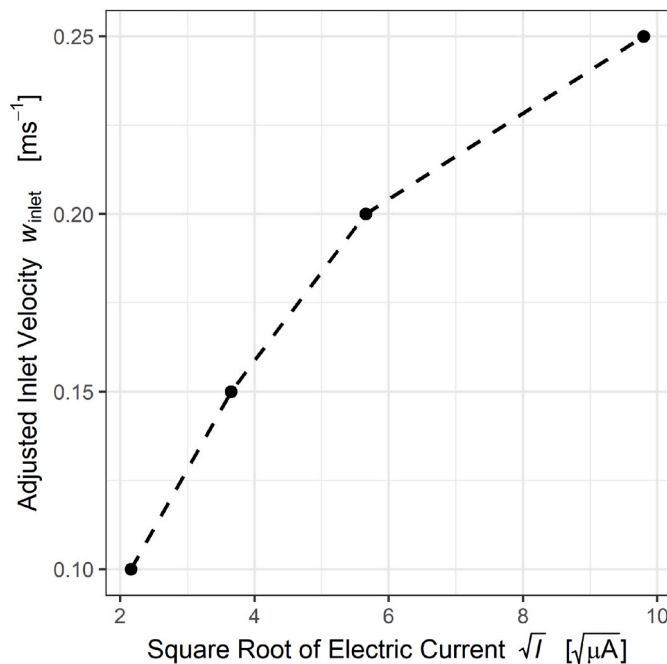


Fig. 20. Relationship between the adjusted inlet velocity (numerically derived) and the square root of electric current (experimentally derived) for the ionic wind amplifier. The plot reveals two distinct linear regimes: an initial regime within the range of $2 \sqrt{\mu A} < \sqrt{I} < 5.7 \sqrt{\mu A}$, which indicates a more efficient conversion of electrical energy into kinetic energy of the airflow. Beyond this range, a higher electric current correlates with a proportionally smaller increase in inlet velocity, suggesting increased charge dissipation.

6. Conclusion

We experimentally investigated a novel prototype of an airflow propulsion device, the ionic wind amplifier, capable of delivering high flow rates with slight pressure rise and energy consumption. The design is compact and scalable, either sequentially or as an array. One ionic wind amplifier unit consists of a core piece housing all the high-voltage electrical components and a cover piece with the Coanda surface responsible for amplifying flow rates. Several variations have been investigated, including different emitter and collector arrangements, Coanda surface shapes, and the number of needles. A CFD-based digital mirror assisted the experiments in retrieving additional flow field data. We obtained extensive volume flow rate, power consumption, and transduction efficiency results. Our key findings are.

- The rod collector configuration slightly outperforms the plate configuration in airflow rate and efficiency. However, both are useful for low-power airflow generation. The plate configuration velocity profile resembles a straight profile flow, while the v2 configuration has higher peaks and lower lows.
- The number of needles has an asymptotic effect on the generated flow rates, implying an attainable upper limit beyond which additional needles no longer provide any flow performance benefits.
- Adding a second sequential stage increases the flow rate by 50 % from $5 \text{ m}^3 \text{ h}^{-1}$ to $7.5 \text{ m}^3 \text{ h}^{-1}$. Similarly, the power consumption increases from 0.4 W to 0.6 W. A third stage has a negligible impact on performance compared to the two stages.
- Divergent walls, such as a convex Coanda surface, improve overall aerodynamic performance. However, the airspeed is near zero in the central part.
- The ideal operational voltage is 15–20 kV, where we find transduction efficiencies of 20 to $10 \text{ m}^3 \text{ h}^{-1} \text{ W}^{-1}$, making it appropriate for low-pressure rise ventilation applications.
- The amplification factor is 2.9–3.4 across 10–30 kV voltage levels. The amplification factor is an efficiency metric illustrating how much more flow rate we obtain than with regular ionic wind alone. Nonetheless, the achieved amplification factor is significantly lower than that of pressurized air-based air amplifiers, which have a factor of roughly 10.

Ionic wind amplifiers have the potential to contribute to more sustainable air distribution and localized airflow generation solutions due to their energy efficiency, noise reduction, and environmental benefits. They could be instrumental in applications requiring precise airflow control, such as data centers, cleanrooms, sterilization, or drying processes, where removing excess heat or maintaining specific conditions is crucial. Further investigations should focus on the durability of tungsten needles and ozone production.

Our prototype study has brought the ionic wind amplifier concept closer to commercialization by raising technological readiness. As the technology advances and matures, the ionic wind amplifier is poised to contribute significantly to sustainable air propulsion solutions.

CRediT authorship contribution statement

Donato Rubinetti: Conceptualization, Data curation, Formal analysis, Investigation, Methodology, Project administration, Resources, Software, Supervision, Validation, Visualization, Writing – original draft, Writing – review & editing. **Kamran Iranshahi:** Methodology, Writing – review & editing. **Daniel Onwude:** Writing – review & editing. **Julien Reymond:** Formal analysis, Investigation. **Amirmohammad Rajabi:** Investigation, Software. **Lei Xie:** Methodology, Writing – review & editing. **Bart Nicolai:** Writing – review & editing. **Thijs Defraeye:** Conceptualization, Funding acquisition, Methodology, Project administration, Supervision, Writing – review & editing.

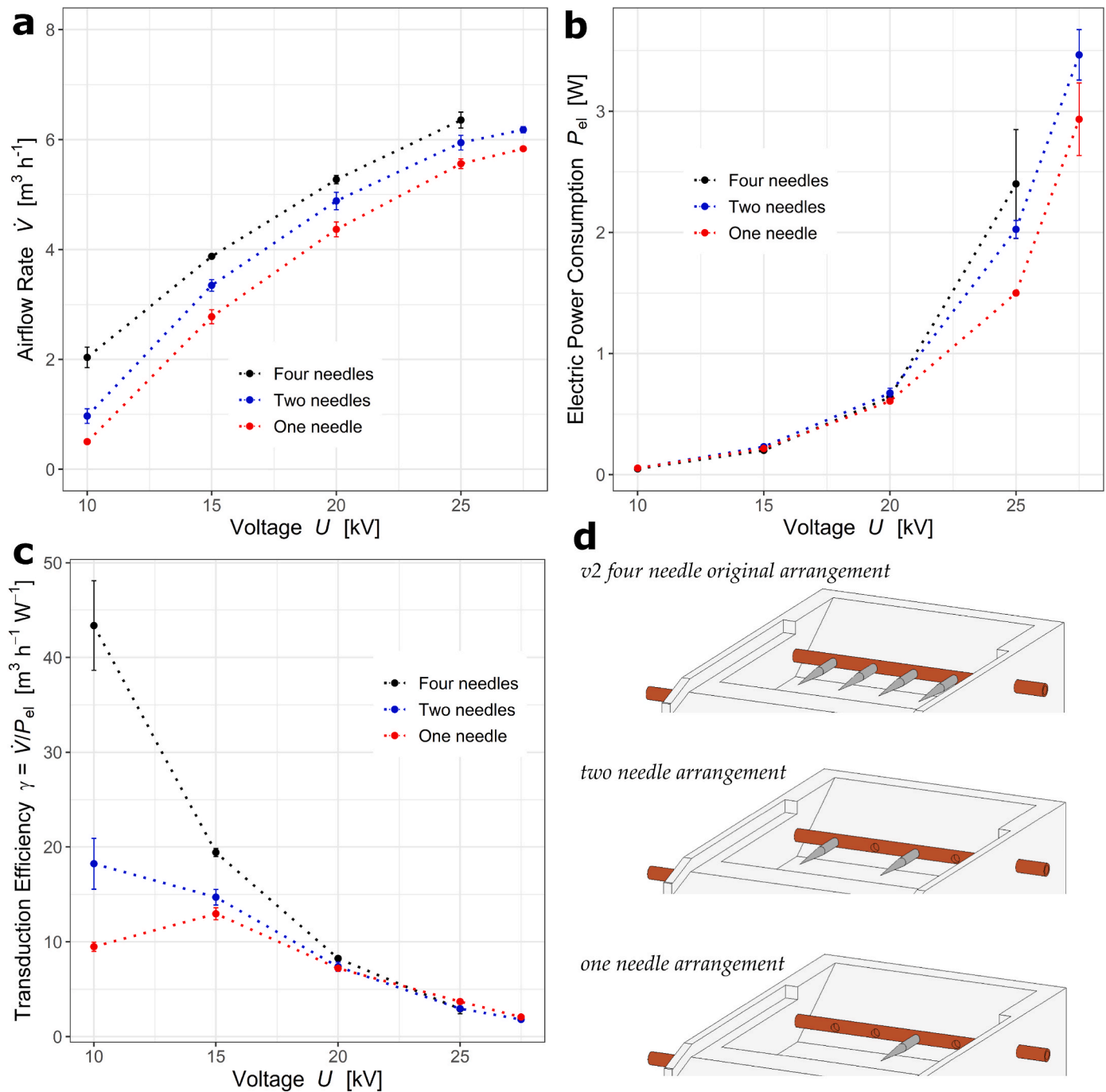


Fig. 21. Performance metrics (airflow rate (a), power consumption (b), and transduction efficiency (c)) as a function of voltage for different numbers of needles (4, 2, and 1) on each side of the ionic wind amplifier. Reducing the number of needles results in a nearly linear decrease in airflow rate across the voltage range. Power consumption remains relatively constant for all needle configurations, with a noticeable difference at 25 kV and beyond, where fewer needles consume less power. The four-needle case performs most efficiently between 10 and 15 kV. In comparison, at 20 kV, the efficiencies of all configurations are almost identical.

Declaration of competing interest

The authors declare that they have no known competing financial interests or personal relationships that could have appeared to influence the work reported in this paper.

Data availability

Data will be made available on request.

Acknowledgments

The authors are grateful to the Swiss Innovation Agency (Innosuisse 34549.1 IP-LS) and Belimed AG for the financial support provided during project conceptualization and execution.

References

- Ambaw, A., et al., 2014. CFD-based analysis of 1-MCP distribution in commercial cool store rooms: porous medium model application. *Food Bioprocess Technol.* 7 (7), 1903–1916. <https://doi.org/10.1007/S11947-013-1190-9/FIGURES/16>.

- Bashkir, I., Martynenko, A., 2021. Optimization of multiple-emitter discharge electrode for electrohydrodynamic (EHD) drying. *J. Food Eng.* 305, 110611 <https://doi.org/10.1016/j.jfoodeng.2021.110611>.
- Chang, Y.J., Peng, J.C., Lin, S.C., Lai, F.C., 2020. Flow induced by an EHD gas pump with secondary emitting electrodes. *J. Electrostat.* 105, 103438 <https://doi.org/10.1016/j.elstat.2020.103438>.
- Chua, K.T., Chou, S.K., Yang, W.M., Yan, J., 2013. Achieving better energy-efficient air conditioning – a review of technologies and strategies. *Appl. Energy* 104, 87–104. <https://doi.org/10.1016/j.apenergy.2012.10.037>.
- Cogollo de Cádiz, M., López Arrabal, A., Díaz Lantada, A., Aguirre, M.V., 2021. Materials degradation in non-thermal plasma generators by corona discharge, 2021 111 Sci. Rep. 11 (1), 1–12. <https://doi.org/10.1038/s41598-021-03447-w>.
- Dau, V.T., Dinh, T.X., Bui, T.T., Terebessy, T., 2016a. Bipolar corona assisted jet flow for fluidic application. *Flow Meas. Instrum.* 50, 252–260. <https://doi.org/10.1016/j.flowmeasinst.2016.07.005>.
- Dau, V.T., Dinh, T.X., Bui, T.T., Tran, C.D., Phan, H.T., Terebessy, T., 2016b. Corona based air-flow using parallel discharge electrodes. *Exp. Therm. Fluid Sci.* 79, 52–56. <https://doi.org/10.1016/j.expthermflusci.2016.06.023>.
- Defraeye, T., Martynenko, A., 2018. Electrohydrodynamic drying of food: new insights from conjugate modeling. *J. Clean. Prod.* 198, 269–284. <https://doi.org/10.1016/j.jclepro.2018.06.250>.
- Dinh, T.X., Lam, D.B., Tran, C.D., Bui, T.T., Pham, P.H., Dau, V.T., 2017. Jet flow in a circulatory miniaturized system using ion wind. *Mechatronics* 47, 126–133. <https://doi.org/10.1016/j.mechatronics.2017.09.007>.
- Dumitrache, A., Frunzulica, F., Ionescu, T.C., 2012. Mathematical modelling and numerical investigations on the Coanda effect. In: *Nonlinearity, Bifurcation and Chaos - Theory and Applications*, InTech.
- Iranshahi, K., Martynenko, A., Defraeye, T., 2020. Cutting-down the energy consumption of electrohydrodynamic drying by optimizing mesh collector electrode. *Energy* 208, 118168. <https://doi.org/10.1016/j.energy.2020.118168>.
- Iranshahi, K., Onwude, D.I., Rubinetti, D., Martynenko, A., Defraeye, T., 2022. Scalable electrohydrodynamic drying configuration for dehydrating biological materials at industrial scale. <https://doi.org/10.31224/2328>.
- Iranshahi, K., Rubinetti, D., Onwude, D.I., Psarianos, M., Schlüter, O.K., Defraeye, T., 2023. Electrohydrodynamic drying versus conventional drying methods: a comparison of key performance indicators. *Energy Convers. Manag.* 279, 116661 <https://doi.org/10.1016/j.enconman.2023.116661>.
- Jewell-Larsen, N.E., Tran, E., Krichtafovitch, I.A., Mamishev, A.V., 2006. Design and optimization of electrostatic fluid accelerators. *IEEE Trans. Dielectr. Electr. Insul.* 13 (1), 191–203. <https://doi.org/10.1109/TDEI.2006.1593417>.
- Jewell-Larsen, N.E., Joseph, G.G., Honer, K.A., 2011. Scaling Laws Electrohydrodynamic Air Movers. <https://doi.org/10.1115/ajtec2011-44626>.
- Johnson, M.J., Go, D.B., 2017. Recent advances in electrohydrodynamic pumps operated by ionic winds: a review. *Plasma Sources Sci. Technol.* 26 (10), 103002 <https://doi.org/10.1088/1361-6595/AA88E7>.
- Johnson, M.J., Tirumala, R., Go, D.B., 2015. Analysis of geometric scaling of miniature, multi-electrode assisted corona discharges for ionic wind generation. *J. Electrostat.* 74, 8–14. <https://doi.org/10.1016/j.elstat.2014.12.001>.
- S. Kanazawa, W. Imagawa, S. Matsunari, S. Akamine, R. Ichiki, and K. Kanazawa, “Ionic Wind Devices Prepared by a 3D Printer.” Accessed: Oct. 14, 2021. [Online]. Available: <https://ijpest.securesite.jp/Contents/11/1/PDF/11-01-038.pdf..>
- Lai, F.C., 2020. EHD gas pumping – a concise review of recent development. *J. Electrostat.* 106, 103469 <https://doi.org/10.1016/j.elstat.2020.103469>.
- Lin, J.H., Lin, S.C., Lai, F.C., 2018. Performance of an electrohydrodynamic gas pump fitted within a nozzle. *J. Electrostat.* 91, 1–8. <https://doi.org/10.1016/j.elstat.2017.11.002>.
- Martynenko, A., Kudra, T., 2016. Electrically-induced transport phenomena in EHD drying - a review. *Elsevier Ltd Trends Food Sci. Technol.* 54, 63–73. <https://doi.org/10.1016/j.tifs.2016.05.019>.
- Monrolin, N., Praud, O., Plouraboué, F., 2018. Electrohydrodynamic ionic wind, force field, and ionic mobility in a positive dc wire-to-cylinders corona discharge in air. *Phys. Rev. Fluids* 3 (6), 1–20. <https://doi.org/10.1103/PhysRevFluids.3.063701>.
- Moreau, E., Touchard, G., 2008. Enhancing the mechanical efficiency of electric wind in corona discharges. *J. Electrostat.* 66 (1–2), 39–44. <https://doi.org/10.1016/j.elstat.2007.08.006>.
- Onma, P., Chantasmri, T., 2018. Comparison of two methods to determine fan performance curves using computational fluid dynamics. *IOP Conf. Ser. Mater. Sci. Eng.* 297 (1), 012026 <https://doi.org/10.1088/1757-899X/297/1/012026>.
- Onwude, D.I., Iranshahi, K., Rubinetti, D., Martynenko, A., Defraeye, T., 2021. Scaling-up electrohydrodynamic drying for energy-efficient food drying via physics-based simulations. *J. Clean. Prod.* 329, 129690 <https://doi.org/10.1016/j.jclepro.2021.129690>.
- Panitz, T., Wasan, D.T., 1972. Flow attachment to solid surfaces: the Coanda effect. *AIChE J.* 18 (1), 51–57. <https://doi.org/10.1002/aic.690180111>.
- Qu, J., et al., 2021. A review on recent advances and challenges of ionic wind produced by corona discharges with practical applications. *J. Phys. D Appl. Phys.* 55 (15), 153002 <https://doi.org/10.1088/1361-6463/AC3E2C>.
- Ramadhan, A.A., Kapur, N., Summers, J.L., Thompson, H.M., 2017a. Numerical analysis and optimization of miniature electrohydrodynamic air blowers. *IEEE Trans. Plasma Sci.* 45 (11), 3007–3018. <https://doi.org/10.1109/TPS.2017.2755365>.
- Ramadhan, A.A., Kapur, N., Summers, J.L., Thompson, H.M., 2017b. Numerical modelling of electrohydrodynamic airflow induced in a wire-to-grid channel. *J. Electrostat.* 87, 123–139. <https://doi.org/10.1016/j.elstat.2017.04.004>.
- Rickard, M., Dunn-Rankin, D., Weinberg, F., Carleton, F., 2006. Maximizing ion-driven gas flows. *J. Electrostat.* 64 (6), 368–376. <https://doi.org/10.1016/j.elstat.2005.09.005>.
- Rubinetti, D., Iranshahi, K., Onwude, D.I., Xie, L., Nicolai, B., Defraeye, T., 2023a. An in-silico proof-of-concept of electrohydrodynamic air amplifier for low-energy airflow generation. *J. Clean. Prod.* 398, 136531 <https://doi.org/10.1016/j.jclepro.2023.136531>.
- Rubinetti, D., Iranshahi, K., Onwude, D., Nicolai, B., Xie, L., Defraeye, T., 2023b. Electrohydrodynamic air amplifier for low-energy airflow generation—an experimental proof-of-concept. *Front. Energy Effic.* 1, 1. <https://doi.org/10.3389/FENERF.2023.1140586>.
- Rubinetti, D., Iranshahi, K., Onwude, D.I., Nicolai, B.M., Xie, L., Defraeye, T., 2024. Energy-saving discharge needle shape for electrohydrodynamic airflow generation. *J. Electrostat.* 127, 103876 <https://doi.org/10.1016/j.jelstat.2023.103876>.
- Shao, Z., Wang, B., Cai, L., Chang, C., Sun, L., 2022. Optical and thermal performance of dynamic concentrating solar module for building integration. *J. Clean. Prod.* 367, 132931 <https://doi.org/10.1016/j.jclepro.2022.132931>.
- Sigmund, R.S., 1982. Simple approximate treatment of unipolar space-charge-dominated coronas: the Warburg law and the saturation current. *J. Appl. Phys.* 53 (2), 891–898. <https://doi.org/10.1063/1.330557>.
- Tien, C.P., Lin, S.C., Lai, F.C., 2020. EHD gas pump in a square channel with electrodes mounted on one wall. *J. Electrostat.* 107, 103482 <https://doi.org/10.1016/j.elstat.2020.103482>.
- Tirumala, R., Go, D.B., 2011. Multi-electrode assisted corona discharge for electrohydrodynamic flow generation in narrow channels. *IEEE Trans. Dielectr. Electr. Insul.* 18 (6), 1854–1863. <https://doi.org/10.1109/TDEI.2011.6118623>.
- Vaddi, R.S., Guan, Y., Mamishev, A., Novoselov, I., 2020. Analytical Model for Electrohydrodynamic Thrust. February.
- Venkatesh, S., Kumar, A., Bhattacharya, A., Pramanik, S., 2021. Ionic wind review-2020: advancement and application in thermal management, 2021 463 Sadhana 46 (3), 1–27. <https://doi.org/10.1007/S12046-021-01687-0>.
- Versteeg, H.K., Malalasekera, W., 2007. *An Introduction to Computational Fluid Dynamics: the Finite Volume Method*. Pearson education.
- Wang, H.C., Jewell-Larsen, N.E., Mamishev, A.V., 2013. Thermal management of microelectronics with electrostatic fluid accelerators. *Pergamon Appl. Therm. Eng.* 51 (1–2), 190–211. <https://doi.org/10.1016/j.applthermaleng.2012.08.068>.
- Wang, J., Jun Liu, Y., Zhu, T., Qiang Chen, Y., bo Wang, J., 2021. Magnetic field enhanced ionic wind for environment-friendly improvement and thermal management application. *Appl. Therm. Eng.* 194, 117054 <https://doi.org/10.1016/j.applthermaleng.2021.117054>.
- Wen, T.Y., Ye, J.C., 2022. On blockage-induced characteristics of transduction efficiency for needle-ring electrohydrodynamic pumps. *J. Electrostat.* 120, 103765 <https://doi.org/10.1016/j.elstat.2022.103765>.
- Wu, Y., et al., 2017. Greener corona discharge for enhanced wind generation with a simple dip-coated carbon nanotube decoration. *J. Phys. D Appl. Phys.* 50 (39), 395304 <https://doi.org/10.1088/1361-6463/AA81A9>.
- Xie, L., Defraeye, T., Rubinetti, D., 2023. ELECTROHYDRODYNAMIC GAS FLOWRATE AMPLIFIER FOR GENERATING A GAS FLOW. *WO 2023/187046 A1*.
- Xu, H., et al., 2018. Flight of an aeroplane with solid-state propulsion, 2018 5637732 Nat 563 (7732), 532–535. <https://doi.org/10.1038/s41586-018-0707-9>.
- Zeng, M.J., Qu, Z.G., Zhang, J.F., 2023. Negative corona discharge and flow characteristics of a two-stage needle-to-ring configuration ionic wind pump for temperature and relative humidity. *Int. J. Heat Mass Tran.* 201, 123561 <https://doi.org/10.1016/j.ijheatmasstransfer.2022.123561>.
- Zhang, J., Lai, F.C., 2011. Effect of emitting electrode number on the performance of EHD gas pump in a rectangular channel. *J. Electrostat.* 69 (6), 486–493. <https://doi.org/10.1016/j.elstat.2011.06.007>.
- Zhang, X., Li, H., 2020. Feasibility analysis for control of bioaerosol concentration at indoor corner via airflow from ventilation outlet with energy optimization. *J. Clean. Prod.* 248 <https://doi.org/10.1016/j.jclepro.2019.119289>.
- Zhang, G.-W., Yang, J.-K., 2021. A review on recent advances and challenges of ionic wind produced by corona discharges with practical applications You may also like Numerical simulation on ionic wind in circular channels. *J. Phys. D Appl. Phys. Top. Rev.* 55, 153002 <https://doi.org/10.1088/1361-6463/ac3e2c>.
- Zhang, J.F., Wu, X.W., Qu, J.G., Zhang, D.W., Qu, Z.G., 2022. Electrohydrodynamic and heat transfer characteristics of a planar ionic wind generator with flat electrodes. *Appl. Therm. Eng.* 211, 118508 <https://doi.org/10.1016/j.applthermaleng.2022.118508>.
- Zhao, L., Adamiak, K., 2016. EHD flow produced by electric corona discharge in gases: from fundamental studies to applications (a review). *Part. Sci. Technol.* 34 (1), 63–71. <https://doi.org/10.1080/02726351.2015.1043677>.
- Zhao, P., Portugal, S., Roy, S., 2015. Efficient needle plasma actuators for flow control and surface cooling. *Appl. Phys. Lett.* 107 (3), 033501 <https://doi.org/10.1063/1.4927051>.
- Zhou, D., Tang, J., Kang, P., Wei, L., Zhang, C., 2018. Effects of magnetic field intensity on ionic wind characteristics. *J. Electrostat.* 96, 99–103. <https://doi.org/10.1016/j.elstat.2018.10.007>.
- RStudio | Open source & professional software for data science teams - RStudio <https://www.rstudio.com/> (accessed March. 18, 2022).